



Late Time Phenomena in $f(T, \mathcal{T})$ Gravity Framework: Role of H_0 Priors

L.K. Duchaniya ^{1,*} and B. Mishra ^{1,†}

¹*Department of Mathematics, Birla Institute of Technology and Science, Pilani,
Hyderabad Campus, Jawahar Nagar, Kapra Mandal, Medchal District, Telangana 500078, India.*

Abstract: This study explored the behavior of the $f(T, \mathcal{T})$ cosmological model with the use of various data set combinations. We also compared the results for this model between the Pantheon+ (without SH0ES) and the Pantheon+&SH0ES (with SH0ES) data sets. Additionally, we incorporated data from BAO along with H_0 priors. We observed that integrating SH0ES data points leads to a higher estimation of H_0 than Pantheon+ (without SH0ES). We perform an extensive MCMC analysis for each combination of data sets, providing constraints on the model parameters. We also computed the χ^2_{min} value for each combination of data sets to evaluate the chosen model against the standard Λ CDM model. Our primary finding is that the various dataset combinations in the $f(T, \mathcal{T})$ model we examined relate to a range of Hubble constants, which could contribute to reducing the cosmic tension associated with this parameter. Additionally, we investigate the evolution of matter fluctuations by solving the density contrast evolution equation numerically. We calculate numerical solutions for the weighted growth rate $f\sigma_8$ using these findings. We plotted the cosmological background parameters to check the behavior of the $f(T, \mathcal{T})$ model in late-time. Based on the behavior of these background cosmological parameters, we conclude that our selected models reflect the late-time cosmic dynamics of the Universe.

I. INTRODUCTION

The late-time cosmic behavior of the Universe has emerged as the most compelling enigmas in contemporary cosmology. Following an extended period of almost uniform expansion, observational evidence revealed that an unidentified energy component is driving spacetime expansion at an accelerating rate [1, 2]. The leading candidate for this phenomenon is dark energy (DE) [3, 4], which has a major share of approximately 70% of the total mass-energy budget of the Universe. As a consequence, it largely influences the ultimate fate of the Universe. The discovery of cosmic acceleration poses profound questions about our understanding of gravity and drives new investigations into the fundamental principles of physics. The Λ CDM model that describes the Universe as a composition of cold dark matter (CDM) and DE represented by a cosmological constant Λ has been corroborated by several cosmological observations [5–10]. However, the discrepancies in Hubble constant H_0 and the structure growth parameter S_8 pose additional challenges. The recent observed values of H_0 show a notable rift between the value derived from early Universe observations such as cosmic microwave background (CMB) via the Planck satellite [11] and gleaned from local measurements utilizing Cepheid variables and Supernovae Type Ia [12]. In particular, Riess et al. [12] within the SH0ES Team have reported a Hubble constant estimate of $73.30 \pm 1.04 \text{ km s}^{-1} \text{ Mpc}^{-1}$, based on Supernovae Type Ia observations. Whereas the H0LiCOW Collaboration [13] derived a value of $73.3^{+1.7}_{-1.8} \text{ km s}^{-1} \text{ Mpc}^{-1}$ through a strong gravitational lensing of quasars. Further, Freedman et al. [14] reported a lower estimate of $69.8 \pm 1.9 \text{ km s}^{-1} \text{ Mpc}^{-1}$, obtained using the tip of the red giant branch (TRGB) as a distance indicator. The Planck Collaboration [15] provides a Hubble constant value of $67.4 \pm 0.5 \text{ km s}^{-1} \text{ Mpc}^{-1}$, while Abbot et al. [16] suggest $67.2^{+1.2}_{-1.0} \text{ km s}^{-1} \text{ Mpc}^{-1}$. This divergence between the estimates from early and late Universe measurements, known as H_0 tension, raises significant questions in modern cosmology. Initially identified with the first release of Planck data [11], the H_0 tension has garnered increasing scrutiny and attention in recent studies [15, 17, 18]. This inconsistency has led to exploring possible modifications to the standard cosmological model and considering new physics beyond Λ CDM. The σ_8 tension refers to a discrepancy of approximately 3σ between the values of σ_8 , which quantifies the amplitude of matter clustering on scales of $8 h^{-1} \text{ Mpc}$. In particular, the σ_8 value inferred from Cosmic Microwave Background (CMB) measurements by [15] is higher than that derived from large-scale structure observations, such as those from SDSS/BOSS [5, 19]. However, recent analyses from the KiDS-1000 collaboration [20, 21]

* duchaniya98@gmail.com

† bivu@hyderabad.bits-pilani.ac.in

and the SRG/eROSITA all-sky survey [22] demonstrate full consistency with the Planck 2018 results [15], suggesting that the previously reported σ_8 tension may be less significant than initially thought.

General relativity (GR) encapsulates the interplay between matter, energy and the curvature of spacetime. However, modifications in GR have been inevitable to address the late-time behavior of the Universe. A simple approach to understanding this phenomenon is the introduction of cosmological constant, leading to the Λ CDM model. Otherwise, GR can be refined by integrating extra terms or scalar fields into the gravitational action. These modifications may include higher-order curvature invariants or scalar fields coupled to the curvature. This may provide a robust theoretical framework that accommodates a concordance model for cosmology through various straightforward adjustments [23, 24]. The modifications can be incorporated as the Einstein-Hilbert action [25, 26] to provide various cosmological phenomena. One such gravitational modification is the torsional equivalent formulation of GR, known as the Teleparallel Equivalent of GR (TEGR) [27, 28]. TEGR permits the formulation of second-order equations in four-dimensional spacetime and employs the Weitzenböck connection [29]. This framework is characterized by four linearly independent tetrad fields, which serve as the orthonormal bases for the tangent space at each point in spacetime, with the torsion tensor being derived from the first derivatives of these tetrads. To note, $f(R)$ gravity [25] presents the basic modification of GR, whereas $f(T)$ [30–37] gravity is the modification of TEGR. Further, many variations of the torsion-influenced gravitational theory such as $f(T, T_G)$ (T_G refers to the Gauss-Bonnet term) [38, 39], $f(T, B)$ [40, 41] (B signifies the boundary term), $f(T, \phi)$ [42–45] (ϕ represents the scalar field) and $f(T, \mathcal{T})$ [46–51] (\mathcal{T} represents trace of energy-momentum tensor) have been proposed.

The H_0 tension refers to the observed discrepancies in the Hubble constant measurements in various observational methodologies, which challenges the standard Λ CDM model [52–61]. The motivation of this study is to examine the influence of H_0 priors in alleviating H_0 tension and late time behavior of the Universe in $f(T, \mathcal{T})$ gravitational theory [46]. The gravitational Lagrangian can be developed in this framework using the torsion scalar T functions and the trace of the energy-momentum tensor \mathcal{T} . The paper is organized as follows: In Sec.-II, we present a brief overview of the mathematical formalism of $f(T, \mathcal{T})$ gravity. The formalism of the cosmological data sets and the mathematical formalism of the statistical criteria for model comparison (AIC and BIC) is defined in Sec.-III. In Sec.-IV, we analyze the cosmological observations for different data set combinations and the H_0 priors. In Sec.-V, we study the growth of matter overdensities under the quasi-static approximation for sub-horizon scales. In Sec.-VI, we present the evolution of the background cosmological parameters to analyze the behavior of the models at late times. We have given a conclusion on the findings in Sec.-VII. The results of cosmological observation for the Λ CDM model are summarized in the appendix.

II. MATHEMATICAL FORMALISM

In teleparallel gravity (TG), the tetrad fields e_μ^A act as dynamical variables in place of the usual metric tensor $g_{\mu\nu}$ in GR. The metric tensor in TG can be represented as,

$$g_{\mu\nu} = \eta_{AB} e_\mu^A e_\nu^B. \quad (1)$$

The Greek indices denote space-time coordinates, while the capital Latin indices indicate tangent space-time coordinates. η_{AB} denotes the Minkowski space-time and the tetrad fields satisfy the orthogonality condition $e^\mu_A e^B_\mu = \delta^B_A$. Employing the Weitzenböck connection as a framework for $f(T, \mathcal{T})$ gravity, we can define

$$\hat{\Gamma}^\lambda_{\nu\mu} \equiv e^\lambda_A (\partial_\mu e^A_\nu + \omega^A_{B\mu} e^B_\nu), \quad (2)$$

where $\omega^A_{B\mu}$ represents a spin connection that guarantees invariance under Lorentz transformations, which stems directly from the indices of the tangent space. The most general spin connection that results in zero curvature is the purely inertial spin connection

$$\omega^A_{B\mu} = \Lambda^A_C \partial_\mu \Lambda^C_B, \quad (3)$$

where Λ^A_C is a local Lorentz transformation matrix. The following represents solely the effects of inertia, as it relies only on the selection of the frame. Nevertheless, it is not uniquely defined because it depends solely on the choice of the observer, signified by a Lorentz matrix. Specifically, different spin connections indicate various inertial effects

for the observer, which do not influence the field equations. On the other hand, the spin connections used in GR are not flat [62] because they depend on the tetrads. In TG, the equations governing motion incorporate both gravitational and local degrees of freedom, depicted by the pair of tetrads and spin connections. Now, the torsion tensor characterized by the anti-symmetric part of the Weitzenböck connection can be described as,

$$T_{\mu\nu}^{\lambda} \equiv \hat{\Gamma}_{\nu\mu}^{\lambda} - \hat{\Gamma}_{\mu\nu}^{\lambda} = e_A^{\lambda} \partial_{\mu} e_{\nu}^A - e_A^{\lambda} \partial_{\nu} e_{\mu}^A. \quad (4)$$

The torsion tensor exhibits covariance under diffeomorphisms and Lorentz transformations. Provided that the torsion tensor has been correctly contracted, the torsion scalar can be represented as,

$$T \equiv \frac{1}{4} T^{\rho\mu\nu} T_{\rho\mu\nu} + \frac{1}{2} T^{\rho\mu\nu} T_{\nu\mu\rho} - T_{\rho\mu}^{\rho} T^{\nu\mu}_{\nu}. \quad (5)$$

The action in TG is based on the teleparallel Lagrangian T and the $f(T)$ gravity extends this Lagrangian to an arbitrary function $f(T)$. The action of $f(T, \mathcal{T})$ gravity [46] is,

$$S = \frac{1}{16\pi G} \int d^4x e [T + f(T, \mathcal{T})] + \int d^4x e \mathcal{L}_m, \quad (6)$$

where \mathcal{L}_m denotes matter Lagrangian and G represents the gravitational constant. The determinant of the tetrad field is expressed as $e = \det[e_{\mu}^A] = \sqrt{-g}$. Varying action (6) with respect to the tetrad field, one can obtain the gravitational field equations for $f(T, \mathcal{T})$ gravity as,

$$\begin{aligned} & [e^{-1} \partial_{\mu} (e e_A^{\rho} S_{\rho}^{\mu\nu}) - e_A^{\lambda} T_{\mu\lambda}^{\rho} S_{\rho}^{\nu\mu}] (1 + f_T) + e_A^{\rho} S_{\rho}^{\mu\nu} [\partial_{\mu}(T) f_{TT} + \partial_{\mu}(\mathcal{T}) f_{T\mathcal{T}}] + \frac{1}{4} e_A^{\nu} [T + f(T)] \\ & - f_{\mathcal{T}} \left(\frac{e_A^{\rho} T_{\rho}^{\nu} + p e_A^{\rho}}{2} \right) = 4\pi G e_A^{\rho} T_{\rho}^{\nu}. \end{aligned} \quad (7)$$

For brevity, we denote $f_T = \frac{\partial f}{\partial T}$, $f_{TT} = \frac{\partial^2 f}{\partial T^2}$, $f_{\mathcal{T}} = \frac{\partial f}{\partial \mathcal{T}}$ and $f_{T\mathcal{T}} = \frac{\partial^2 f}{\partial T \partial \mathcal{T}}$. The total energy-momentum tensor can be represented as T_{ρ}^{ν} . The superpotential, $S_{\rho}^{\mu\nu} \equiv \frac{1}{2} (K^{\mu\nu}_{\rho} + \delta_{\rho}^{\mu} T^{\alpha\nu}_{\alpha} - \delta_{\rho}^{\nu} T^{\alpha\mu}_{\alpha})$. The contortion tensor in the superpotential can be defined as, $K^{\mu\nu}_{\rho} \equiv \frac{1}{2} (T^{\nu\mu}_{\rho} + T_{\rho}^{\mu\nu} - T^{\mu\nu}_{\rho})$.

We consider the homogeneous and isotropic flat Friedmann-Lemaître-Robertson-Walker (FLRW) space-time as,

$$ds^2 = dt^2 - a^2(t) [dx^2 + dy^2 + dz^2], \quad (8)$$

where $a(t)$ denotes the scale factor that represents the rate of expansion in the spatial dimensions. From Eq. (5), the torsion scalar can be derived as,

$$T = -6H^2, \quad (9)$$

and the associated tetrad field can be expressed as $e_{\mu}^A \equiv \text{diag}(1, a(t), a(t), a(t))$. We can now derive the field equations for $f(T, \mathcal{T})$ gravity Eq. (7) as,

$$3H^2 = 8\pi G \rho_m - \frac{1}{2} (f + 12H^2 f_T) + f_{\mathcal{T}} (\rho_m + p_m), \quad (10)$$

$$\dot{H} = -4\pi G (\rho_m + p_m) - \dot{H} (f_T - 12H^2 f_{TT}) - H (\dot{\rho}_m - 3\dot{p}_m) f_{T\mathcal{T}} - f_{\mathcal{T}} \left(\frac{\rho_m + p_m}{2} \right). \quad (11)$$

An over dot represents ordinary derivative with respect to cosmic time t . The trace of the energy-momentum tensor, $\mathcal{T} = \rho_m - 3p_m$, where p_m denotes the matter pressure and ρ_m be the corresponding energy density term. The Friedmann Eqs.(10-11) can be written as,

$$3H^2 = 8\pi G (\rho_m + \rho_{DE}), \quad (12)$$

$$-2\dot{H} = 8\pi G (\rho_m + p_m + \rho_{DE} + p_{DE}). \quad (13)$$

From Eqs. (10-13), the energy density (ρ_{DE}) and pressure (p_{DE}) for the DE component can be retrieved as,

$$\rho_{DE} \equiv -\frac{1}{16\pi G} \left[f + 12H^2 f_T - 2f_T(\rho_m + p_m) \right], \quad (14)$$

$$p_{DE} \equiv (\rho_m + p_m) \left[\frac{1 + \frac{f_T}{8\pi G}}{1 + f_T - 12H^2 f_{TT} + H \frac{d\rho_m}{dH} (1 - 3c_s^2) f_{TT}} - 1 \right] + \frac{1}{16\pi G} [f + 12H^2 f_T - 2f_T(\rho_m + p_m)]. \quad (15)$$

The behavior of the total EoS parameter (ω_{tot}) and the deceleration parameter (q) are significant to analyze the late time behavior of the Universe and can be expressed as,

$$\omega_{tot} = \frac{p_m + p_{DE}}{\rho_m + \rho_{DE}} \equiv -1 - \frac{2\dot{H}}{3H^2}, \quad (16)$$

$$q = \frac{1}{2}(1 + 3\omega_{tot}). \quad (17)$$

III. COSMOLOGICAL OBSERVATION DATA SETS

We have presented brief descriptions of the cosmological data sets and the methodology. The data sets to be used are Hubble, Supernovae Type Ia and BAO. The H_0 priors used are R21 and TRGB. We shall use the emcee package Ref [63] to execute a Markov Chain Monte Carlo (MCMC) analysis to integrate these data sets. MCMC is a robust sampling technique that extracts samples from the posterior distribution of the cosmological model. This method is widely used in Bayesian statistics to estimate model parameters and quantify uncertainties. A large sample size would be required to ensure the accuracy of the model in this process. We compute the one-dimensional parameter distribution that provides the posterior distribution of each parameter and the two-dimensional parameter distributions, revealing the covariance relationship between pairs of parameters. Our analysis culminates in generating MCMC corner plots at 1σ and 2σ confidence levels.

Cosmic Chronometers (CC): We employed 31 data points for the Hubble parameter derived from the cosmic chronometer (CC) methodology. This technique allows for directly analyzing the Hubble function across a range of redshifts up to $z \leq 2$. The strength of CC data lies in its ability to evaluate the age difference between two passively evolving galaxies that formed simultaneously but have a small difference in redshift, enabling the calculation of $\frac{\Delta z}{\Delta t}$. Refs [64–71] provide the basis for the CC data points. The associated estimate for χ_{CC}^2 is given as,

$$\chi_{CC}^2 = \Delta H(z_i, \Theta)^T C_{CC}^{-1} \Delta H(z_i, \Theta), \quad (18)$$

where $\Delta H(z_i, \Theta) = H(z_i, \Theta) - H_{\text{obs}}(z_i)$ and C_{CC}^{-1} is the covariance matrix provided in [72]. The term $H(z_i, \Theta)$ represents the theoretical values of the Hubble parameter at a specific redshift z_i , while $H_{\text{obs}}(z_i)$ denotes the observed values of the Hubble parameter at z_i .

Pantheon+ Supernovae Type Ia (SNIa) dataset : We utilize the 1701 data points obtained from the Pantheon+ sample [12, 73, 74], which records the apparent distances of 1550 different Supernovae Ia (SNIa) occurrences within a redshift range of $0.01 < z < 2.3$. The distance modulus function is the discrepancy between the apparent magnitude m and the absolute magnitude M . The Pantheon+ dataset incorporates SH0ES measurements of Cepheid distances to simultaneously ascertain H_0 and M without including a prior in the parameters. From this point forward, this data set will be called PN⁺. In our evaluation, we examined the PN⁺ dataset together with the SH0ES data point and without it. At a redshift z_i , the distance modulus function $\mu(z_i, \Theta)$ can be formulated as

$$\mu(z_i, \Theta) = m - M = 5 \log_{10} [D_L(z_i, \Theta)] + 25, \quad (19)$$

the luminosity distance $D_L(z_i, \Theta)$ can be formulated as

$$D_L(z_i, \Theta) = c(1 + z_i) \int_0^{z_i} \frac{dz'}{H(z', \Theta)}, \quad (20)$$

where c denotes the speed of light. To determine the chi-square (χ_{SN}^2) value with the PN^+ & $SH0ES$ compilation, which includes 1701 Supernovae data points, we apply the following formula[75]:

$$\chi_{\text{SN}}^2 = (\Delta\mu(z_i, \Theta))^T C^{-1} (\Delta\mu(z_i, \Theta)) . \quad (21)$$

In this context, C refers to the covariance matrix incorporating systematic and statistical uncertainties in the measurements. Additionally, $\Delta\mu(z_i, \Theta) = \mu(z_i, \Theta) - \mu(z_i)_{\text{obs}}$ indicates the disparity between the predicted and observed distance modulus at the redshift z_i .

BAO data set: We also analyze a combined baryon acoustic oscillation (BAO) data set of distinct data points. We utilize a BAO data set that features observations from the Six-degree Field Galaxy Survey at an effective redshift of $z_{\text{eff}} = 0.106$ [76], the BOSS DR11 quasar Lyman-alpha measurements at $z_{\text{eff}} = 2.4$ [77] and the SDSS Main Galaxy Sample at $z_{\text{eff}} = 0.15$ [78]. Additionally, we incorporate measurements of $H(z)$ and angular diameter distances obtained from the SDSS-IV eBOSS DR14 quasar survey at effective redshifts $z_{\text{eff}} = \{0.98, 1.23, 1.52, 1.94\}$ [79], along with the consensus BAO measurements of the Hubble parameter and the corresponding comoving angular diameter distances from SDSS-III BOSS DR12 at $z_{\text{eff}} = \{0.38, 0.51, 0.61\}$ [5]. Our analysis considers the complete covariance matrix for the sets of BAO data. To evaluate the BAO data set for the cosmological model, it is necessary to establish the Hubble distance $D_H(z)$, the comoving angular diameter distance $D_M(z)$ and the volume-average distance $D_V(z)$.

$$D_H(z) = \frac{c}{H(z)}, \quad D_M(z) = (1+z)D_A(z), \quad D_V(z) = \left[(1+z)^2 D_A^2(z) \frac{z}{H(z)} \right]^{1/3}, \quad (22)$$

where $D_A(z) = (1+z)^{-2}D_L(z)$ denotes the angular diameter distance. To include the BAO findings in MCMC analyses, we need to take into account the pertinent combinations of parameters:

$$\mathcal{F}(z_i) = \left\{ \frac{D_V(z_i)}{r_s(z_d)}, \frac{r_s(z_d)}{D_V(z_i)}, D_H(z_i), D_M(z_i) \left(\frac{r_{s,\text{fid}}(z_d)}{r_s(z_d)} \right), H(z_i) \left(\frac{r_s(z_d)}{r_{s,\text{fid}}(z_d)} \right), D_A(z_i) \left(\frac{r_{s,\text{fid}}(z_d)}{r_s(z_d)} \right) \right\}, \quad (23)$$

where $r_s(z_d)$ represents the sound horizon at the drag epoch, while $r_{s,\text{fid}}(z_d)$ indicates the fiducial sound horizon. To accomplish this, we calculated the comoving sound horizon $r_s(z)$ at the redshift $z_d \approx 1059.94$ [15], which corresponds to the conclusion of the baryon drag epoch.

$$r_s(z) = \int_z^\infty \frac{c_s(\tilde{z})}{H(\tilde{z})} d\tilde{z} = \frac{1}{\sqrt{3}} \int_0^{1/(1+z)} \frac{da}{a^2 H(a) \sqrt{1 + \left[\frac{3\Omega_{b,0}}{4\Omega_{\gamma,0}} \right] a}}, \quad (24)$$

where the subsequent values are utilized: $\Omega_{b,0} = 0.02242$ [15], $T_0 = 2.7255 \text{ K}$ [80] and a reference value of $r_{s,\text{fid}}(z_d) = 147.78 \text{ Mpc}$. The relevant estimate for χ_{BAO}^2 is given by [75],

$$\chi_{\text{BAO}}^2(\Theta) = (\Delta\mathcal{F}(z_i, \Theta))^T C_{\text{BAO}}^{-1} \Delta\mathcal{F}(z_i, \Theta), \quad (25)$$

where C_{BAO} denotes the covariance matrix for the chosen BAO data and $\Delta\mathcal{F}(z_i, \Theta) = \mathcal{F}(z_i, \Theta) - \mathcal{F}_{\text{obs}}(z_i)$ indicates the discrepancy between the theoretical and measured values of \mathcal{F} at redshift z_i .

We will investigate how an H_0 prior affects the selected functional form $f(T, \mathcal{T})$ along with the previously described data set. We will consider the recent local measurement from $SH0ES$ which gives $H_0 = 73.04 \pm 1.04 \text{ km s}^{-1} \text{ Mpc}^{-1}$ (R21) [12]. The measurement using the tip of the red giant branch (TRGB) as a standard candle with $H_0 = 69.8 \pm 1.9 \text{ km s}^{-1} \text{ Mpc}^{-1}$ [14].

We analyze the effectiveness of the cosmological model and dataset by computing their respective minimum χ_{min}^2 values, which are derived from the maximum likelihood L_{max} , using the formula $\chi_{\text{min}}^2 = -2 \ln L_{\text{max}}$. Additionally, we compare the model against the standard ΛCDM by applying the Akaike Information Criteria (AIC), which takes into account both the quality of the fit (evaluated via χ_{min}^2) and the complexity of the model (indicated by the number of parameters k). The AIC is formulated as

$$\text{AIC} = \chi_{\text{min}}^2 + 2k, \quad (26)$$

A smaller AIC value indicates that a model provides a better fit for the data while considering its complexity. The AIC imposes a penalty on models with a greater number of parameters, even if they demonstrate a better fit to the data. Therefore, a model with a lower AIC is preferred over one with a higher AIC, as long as the difference in AIC is significant enough.

In addition, we examine the Bayesian Information Criterion (BIC), which is similar to AIC but gives more weight to the complexity of the model than AIC does, and is expressed as

$$\text{BIC} = \chi_{\min}^2 + k \ln N. \quad (27)$$

In this scenario, N denotes the quantity of samples within the observational data set. The BIC serves the same purpose as the AIC: to find a balance between the accuracy of the model concerning the data and its complexity. However, the BIC applies a stricter penalty on models with more parameters than the AIC due to its dependence on the logarithm of the sample size. Consequently, the penalty for adding parameters becomes more significant as the sample size increases. Comparing the BIC values of two models can help determine which model aligns better with the data, with lower BIC values being favored, provided there is a notable difference.

To assess the performance of models using different combinations of data sets, we calculate the differences in AIC and BIC between the model and the reference model, ΛCDM . The constrained parameters for the ΛCDM model for each combination of data sets are outlined in Appendix VIII. Lower values of ΔAIC and ΔBIC suggest that the chosen model with the data set corresponds more closely to the ΛCDM model, indicating better performance. The quantities ΔAIC , and ΔBIC can be defined as,

$$\Delta\text{AIC} = \Delta\chi_{\min}^2 + 2\Delta k, \quad (28)$$

$$\Delta\text{BIC} = \Delta\chi_{\min}^2 + \Delta k \ln N. \quad (29)$$

IV. COSMOLOGICAL MODEL

In this section, we present and evaluate the results following the methodology described in Sec III, using cosmological observations datasets. We showcase contour plots of the constrained parameters and their respective 1σ and 2σ uncertainties, accompanied by tables summarizing the final results. In all tables and posterior plots, we include results for the Hubble constant H_0 , the current matter density parameter Ω_{m0} and the parameters of the models. This will enable us to examine how the independent data sets and cosmological models influence the Hubble tension. We will briefly highlight the most significant findings, emphasizing the PN^+ (without SH0ES) and PN^+ & SH0ES (with SH0ES) distinctions. In the Friedmann equations [Eq.(10)-Eq.(11)], we need to incorporate some functional form of $f(T, \mathcal{T})$. In this setting, we have considered the following form of $f(T, \mathcal{T})$ [46]

$$f(T, \mathcal{T}) = \alpha T^n \mathcal{T} + \Lambda, \quad (30)$$

where $\alpha \neq 0$, $n \neq 0$ and Λ are arbitrary constants. At present, one can express the Friedmann Eq. (10) as,

$$\alpha = \frac{2 - 2\Omega_{m0} + \frac{\Lambda}{3H_0^2}}{(1 + 2n)\Omega_{m0}(-6H_0^2)^{-n}}, \quad (31)$$

where H_0 and Ω_{m0} respectively represent the Hubble parameter and matter density parameter at present time. From Eq. (31), it can be inferred that the model parameter α depends on other parameters such as $\{H_0, \Omega_{m0}, n \text{ and } \Lambda\}$. By defining the dimensionless Hubble parameter $E(z) = \frac{H(z)}{H_0}$, the Friedmann Eq. (10) for this model can be reformulated as

$$E^2(z) = (1+z)^3\Omega_{m0} - \frac{\Lambda}{6H_0^2} + \left(1 - \Omega_{m0} + \frac{\Lambda}{6H_0^2}\right)(1+z)^3E^{2n}(z). \quad (32)$$

To ensure that the term $\frac{\Lambda}{6H_0^2}$ remains dimensionless, we define the parameter as $\Lambda = H_0^2$. Now, Eq. (32) becomes,

$$E^2(z) = (1+z)^3\Omega_{m0} - \frac{1}{6} + \left(1 - \Omega_{m0} + \frac{1}{6}\right)(1+z)^3E^{2n}(z). \quad (33)$$

Eq. (33) is an implicit formulation for $E(z)$. Considering that analytical solutions for Eq. (33) are impractical, we have adhered to the numerical methods to compute the parameters. The methodology used as described in Sec.-III and the results obtained are described below.

In Fig.-1, we have presented the 1σ and 2σ confidence levels along with the posterior distributions for the parameters H_0 , Ω_{m0} , n and M using CC, PN^+ (without SH0ES) and BAO data sets in addition to the R21 and TRGB priors. It displays the marginalized posterior distributions for different combinations of parameters. The inner contours indicate the 68% confidence level while the outer contours represent the 95% confidence level. This visual representation facilitates a thorough evaluation of parameter uncertainties and correlations. The most noticeable aspect of the findings is the influence these priors exert on H_0 values, as it is clear that these priors generally lead to an increase in the Hubble constant value when contrasted with the scenario of no priors. Including priors decreases the estimated value of Ω_{m0} , albeit to a lesser degree than the impact observed on H_0 . This reduction is expected, as the priors effectively adjust the value of H_0 . Table-I summarizes the results derived from Fig.-1. Notably, the highest value of H_0 is obtained from the data set combination CC+ PN^+ +R21, while the lowest is observed for CC+BAO. The diminished H_0 in the CC+BAO combination can be attributed to incorporating the BAO data set, which originates from early Universe measurements. Furthermore, the nuisance parameter M remains unconstrained in the CC+BAO analysis due to the absence of the PN^+ data set. The determined value of H_0 for the CC+ PN^+ +R21 aligns with the elevated H_0 value reported by the SH0ES team (R22), which states $H_0 = 73.30 \pm 1.04 \text{ km s}^{-1} \text{ Mpc}^{-1}$ [12].

In Fig.-2, we display the 1σ and 2σ confidence intervals alongside the posterior distributions for the parameters H_0 , Ω_{m0} , n and M utilizing the CC, PN^+ &SH0ES (with SH0ES), and BAO datasets, in addition to the R21 and TRGB priors. In Table-III, it is observed that the highest H_0 value is noted for the combination of data sets CC+ PN^+ &SH0ES+R21, which is $H_0 = 72.74^{+0.77}_{-0.74} \text{ km s}^{-1} \text{ Mpc}^{-1}$. The addition of SH0ES data points alongside the PN^+ data set raises the H_0 value in comparison to using only the PN^+ data set (without SH0ES). Integrating the BAO data set results in a lower H_0 value than the combination of the PN^+ & SH0ES data sets. The value of H_0 for inclusion with the BAO data set is consistent with the Planck Collaboration [15], which reports a Hubble constant of $67.4 \pm 0.5 \text{ km s}^{-1} \text{ Mpc}^{-1}$. In contrast, Aboot et al. [16] propose a value of $67.2^{+1.2}_{-1.0} \text{ km s}^{-1} \text{ Mpc}^{-1}$. In this research, we have analyzed the differences between the PN^+ (without SH0ES) and PN^+ & SH0ES (with SH0ES) datasets, also incorporating the BAO dataset and H_0 priors. The findings can be observed in Tables-III and Table-I. From the results, we concluded that including the SH0ES data points with the PN^+ dataset raises the H_0 value compared to PN^+ , which in turn caused adjustments in Ω_{m0} and n due to the change in the H_0 value. Our results for the Hubble constant H_0 value from the data set combination PN^+ (without SH0ES) and PN^+ & SH0ES (with SH0ES), along with the BAO data set combination, align with the findings presented by Brout et al.[56] for the PN^+ (without SH0ES) and PN^+ & SH0ES (with SH0ES).

We have also computed the AIC and BIC values, providing a statistical foundation for selecting the appropriate model. Results related to the Λ CDM model can be found in the Appendix, particularly in Table-VII. Lower values of ΔAIC and ΔBIC suggest that the model using the chosen data sets closely resembles the Λ CDM model. In Tables II and IV, we present the statistical results including χ^2_{\min} , ΔAIC , and ΔBIC for PN^+ (without SH0ES) and PN^+ & SH0ES (with SH0ES), respectively. In this analysis, the values of ΔAIC and ΔBIC for the data set combinations for CC+ PN^+ and CC+ PN^+ &SH0ES that include H_0 priors are notably lower than those for the BAO data set combinations that also incorporate H_0 priors. The study indicates that our model for dataset combination of CC+ PN^+ and CC+ PN^+ &SH0ES performs more effectively than when BAO data is included in combination with the standard Λ CDM model. In fact, for the scenario where the statistical distance deviates most from Λ CDM, specifically for the inclusion of the BAO data set, the statistical criteria yield a negative result, suggesting a slight preference for the model. In contrast, the other scenarios slightly inclined towards the standard cosmological model. The lower value of the ΔAIC and ΔBIC values for the dataset combination with H_0 priors signify that the particular data combination aligns more closely with the standard Λ CDM model.

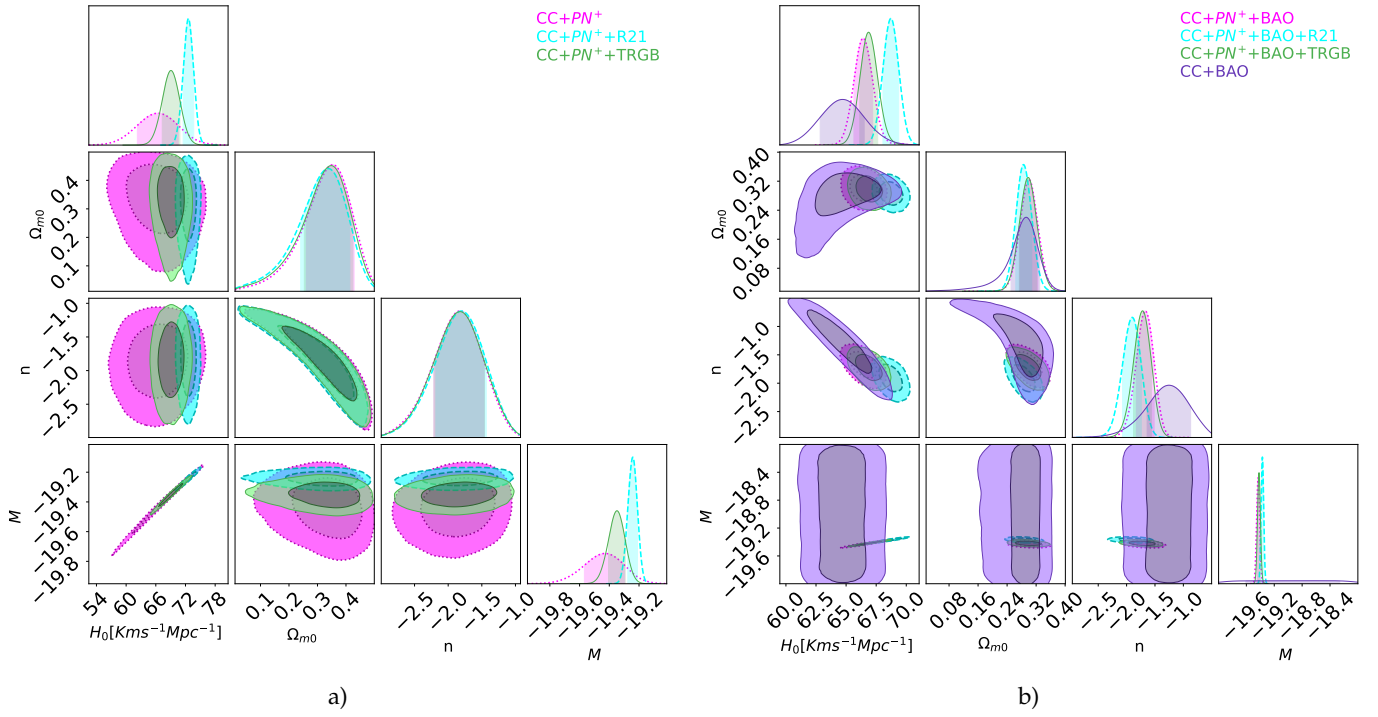


Figure 1: The contour plot of 1 σ and 2 σ uncertainty regions and posterior distribution for the model parameters with the combination of data sets (a) CC, PN^+ (b) CC, PN^+ and BAO. The H_0 priors are: TRGB (Green) and R21 (Cyan).

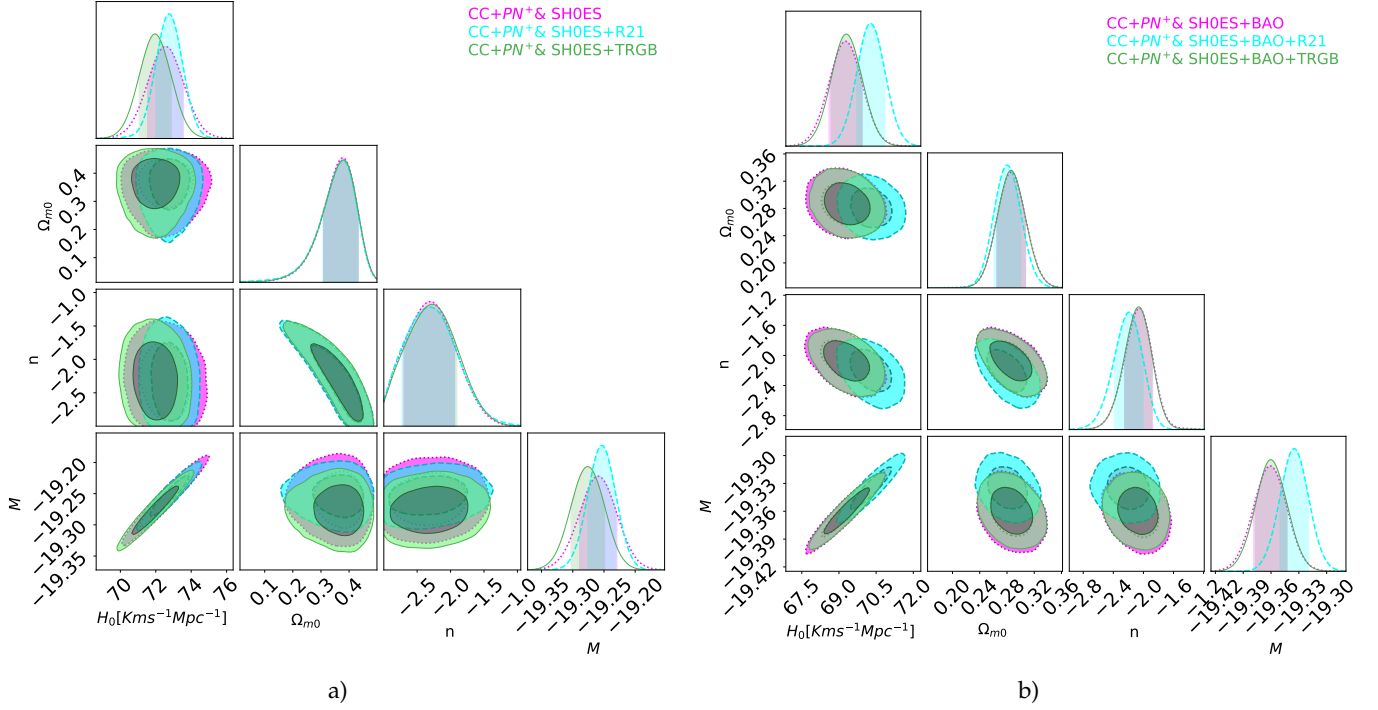


Figure 2: The contour plot of 1 σ and 2 σ uncertainty regions and posterior distribution for the model parameters with the combination of data sets (a) CC, PN^+ & SH0ES (b) CC, PN^+ & SH0ES and BAO. The H_0 priors are: TRGB (Green) and R21 (Cyan).

Table I: The best-fit values of the parameters explored by MCMC analysis. The first column enumerates a combination of data sets with the H_0 priors. The second column presents the constrained H_0 values. The third column contains the constrained Ω_{m0} values. The fourth and fifth columns represent the optimal n and M values respectively. **(Without SH0ES data points)**

Data set	$H_0[\text{km s}^{-1} \text{Mpc}^{-1}]$	Ω_{m0}	n	M
CC+PN ⁺	66.4 ± 4.1	$0.354^{+0.074}_{-0.094}$	$-1.82^{+0.36}_{-0.39}$	$-19.43^{+0.13}_{-0.14}$
CC+PN ⁺ +R21	$72.6^{+1.1}_{-1.0}$	$0.338^{+0.076}_{-0.096}$	$-1.80^{+0.37}_{-0.38}$	$-19.242^{+0.032}_{-0.033}$
CC+PN ⁺ +TRGB	69.1 ± 1.8	$0.347^{+0.077}_{-0.093}$	$-1.82^{+0.36}_{-0.39}$	$-19.348^{+0.055}_{-0.057}$
CC+PN ⁺ +BAO	66.43 ± 0.78	0.300 ± 0.025	$-1.67^{+0.15}_{-0.16}$	$-19.431^{+0.022}_{-0.023}$
CC+PN ⁺ +BAO+R21	$68.73^{+0.64}_{-0.67}$	$0.285^{+0.023}_{-0.021}$	$-1.90^{+0.16}_{-0.17}$	$-19.370^{+0.019}_{-0.018}$
CC+PN ⁺ +BAO+TRGB	$66.88^{+0.75}_{-0.74}$	$0.298^{+0.025}_{-0.024}$	$-1.72^{+0.15}_{-0.16}$	$-19.419^{+0.022}_{-0.021}$
CC+BAO	64.7 ± 1.8	$0.292^{+0.038}_{-0.041}$	-1.25 ± 0.38	-

Table II: The statistical comparison between the chosen model and the standard Λ CDM model. Details regarding the Λ CDM model are given in [Appendix](#). The first column enumerates the data sets including the H_0 priors. The second column displays the values of χ^2_{\min} . The third and fourth column respectively provides the value of AIC and BIC. The fifth and sixth column respectively illustrates the values of ΔAIC and ΔBIC . **(Without SH0ES data points)**

data set	χ^2_{\min}	AIC	BIC	ΔAIC	ΔBIC
CC+PN ⁺	1787.76	1795.76	1800.71	-2.54	-1.31
CC+PN ⁺ +R21	1780.52	1798.52	1803.48	-3.12	-1.87
CC+PN ⁺ +TRGB	1788.41	1796.41	1801.37	-2.79	-1.55
CC+PN ⁺ +BAO	1798.26	1806.26	1811.08	-17.49	-16.28
CC+PN ⁺ +BAO+R21	1524.96	1832.96	1837.78	-0.2	1
CC+PN ⁺ +BAO+TRGB	1801.01	1809.01	1813.83	-14.99	-13.78
CC+BAO	15.98	23.98	28.80	-2.16	-0.96

Table III: The best-fit values of the parameters explored by MCMC analysis. The first column enumerates a combination of data sets with the H_0 priors. The second column presents the constrained H_0 values. The third column contains the constrained Ω_{m0} values. The fourth and fifth columns represent the optimal n and M values respectively. **(With SH0ES data points)**

Data set	$H_0[\text{km s}^{-1} \text{Mpc}^{-1}]$	Ω_{m0}	n	M
CC+PN ⁺ &SH0ES	72.5 ± 1.0	$0.379^{+0.053}_{-0.069}$	$-2.30^{+0.36}_{-0.41}$	-19.260 ± 0.030
CC+PN ⁺ &SH0ES+R21	$72.74^{+0.77}_{-0.74}$	$0.378^{+0.055}_{-0.071}$	$-2.31^{+0.38}_{-0.42}$	$-19.254^{+0.023}_{-0.022}$
CC+PN ⁺ &SH0ES+TRGB	$71.96^{+0.91}_{-0.90}$	$0.381^{+0.052}_{-0.071}$	$-2.27^{+0.36}_{-0.42}$	-19.276 ± 0.027
CC+PN ⁺ &SH0ES+BAO	$69.26^{+0.68}_{-0.66}$	$0.286^{+0.022}_{-0.021}$	$-2.05^{+0.17}_{-0.20}$	$-19.361^{+0.018}_{-0.017}$
CC+PN ⁺ &SH0ES+BAO+R21	$70.28^{+0.59}_{-0.56}$	$0.280^{+0.020}_{-0.019}$	$-2.19^{+0.18}_{-0.20}$	-19.335 ± 0.015
CC+PN ⁺ &SH0ES+BAO+TRGB	$69.30^{+0.63}_{-0.62}$	0.286 ± 0.021	$-2.06^{+0.18}_{-0.19}$	-19.360 ± 0.017

Table IV: The statistical comparison between the chosen model and the standard Λ CDM model. Details regarding the Λ CDM model are given in [Appendix](#). The first column enumerates the data sets including the H_0 priors. The second column displays the values of χ^2_{\min} . The third and fourth column respectively provides the value of AIC and BIC. The fifth and sixth column respectively illustrates the values of Δ AIC and Δ BIC. **(With SH0ES data points)**

data set	χ^2_{\min}	AIC	BIC	Δ AIC	Δ BIC
CC+PN ⁺ &SH0ES	1538.29	1546.29	1551.25	1.07	2.32
CC+PN ⁺ &SH0ES+R21	1538.41	1546.41	1551.37	1.16	2.41
CC+PN ⁺ &SH0ES+TRGB	1539.99	1547.99	1552.92	0.81	2.03
CC+PN ⁺ &SH0ES+BAO	1571.27	1579.27	1584.25	6.1	7.35
CC+PN ⁺ &SH0ES+BAO+R21	1580.95	1588.95	1593.92	12.99	14.25
CC+PN ⁺ &SH0ES+BAO+TRGB	1571.35	1579.35	1584.32	5.85	7.09

V. LINEAR MATTER PERTURBATIONS AND LARGE-SCALE STRUCTURE EVOLUTION

Cosmological models that do not account for interactions within the dark sector, the fundamental equation that governs the growth of matter perturbations in the linear regime at sub-horizon scales during the matter era is [\[81–87\]](#),

$$\ddot{\delta}_m + 2H\dot{\delta}_m = 4\pi G_{eff}\rho_m\delta, \quad (34)$$

where the matter overdensity can be defined as $\delta_m \equiv \frac{\delta\rho_m}{\rho_m}$. In the context of Eq. (34), the effective Newton's constant is introduced as $G_{eff}(a) = G P(a)$, where G is the gravitational constant defined in the action of the theory. This formulation accounts for modifications to gravity. The underlying gravitational theory determines the specific form of $P(a)$. In case of GR, we find that $G_{eff}(a) = G$, which corresponds to $P(a) = 1$. Consequently, Eq. (34) simplifies to yield the standard evolution equation for matter density perturbations [\[88\]](#).

So, it is clear that we can use this general perturbation approach in the context of $f(T, \mathcal{T})$ cosmology, provided the form of $G_{eff}(a)$ is known, or equivalently $P(a)$, in $f(T, \mathcal{T})$ gravity. It can be demonstrated with relative ease that for $f(T, \mathcal{T})$ gravity [\[46, 49\]](#).

$$P(a) = \frac{G_{eff}}{G} = \frac{1}{1 + f_T} \left(1 + \frac{f_T}{2} \right). \quad (35)$$

Eq. (34) can also be rewritten as

$$\delta_m'' + \left(2 + \frac{H'}{H} \right) \delta_m' - \frac{3}{2G} G_{eff} \Omega_m \delta_m = 0. \quad (36)$$

In Eq. (36) prime (') denotes the derivative for $\log(a)$. By incorporating the growth rate of matter fluctuations defined as $f_\delta \equiv \frac{\delta_m'}{\delta_m}$, we can express Eq. (36) in a different form as,

$$f_\delta' + f_\delta^2 + \left(2 + \frac{H'}{H} \right) f_\delta - \frac{3}{2G} G_{eff} \Omega_m = 0. \quad (37)$$

Where $\Omega_m = \frac{\Omega_{m0} a^{-3}}{E^2(a)}$. The measurable $f\sigma_8(z)$ contrasts theoretical predictions with observations data and is specified as

$$f\sigma_8(z) \equiv f_\delta(a) \cdot \sigma(a) = \frac{\sigma_8}{\delta_m(1)} a \delta_m'(a), \quad (38)$$

where $\sigma(a) = \sigma_8 \delta_m(a) / \delta_m(1)$ represents the amplitude of fluctuations in the matter density within spheres measuring $8 h^{-1} \text{ Mpc}$ ($k \sim k_{\sigma_8} = 0.125 h \text{ Mpc}^{-1}$), with $\sigma_8 = \sigma(1)$ being significantly impacted by late-time cosmic expansion and dark energy models [\[89, 90\]](#). Discrepancies in the Λ CDM framework, especially concerning H_0 and σ_8 , arise because large-scale structure (LSS) observations indicate $f\sigma_8$ values are roughly 8% lower than anticipated. This implies that the Λ CDM model might overestimate σ_8 given the same current growth rate $f_\delta(1)$ [\[91\]](#). Nevertheless, since $f_\delta(a)$ depends on the specific model [\[92\]](#), a reduced growth rate might also enhance compatibility with the LSS observations.

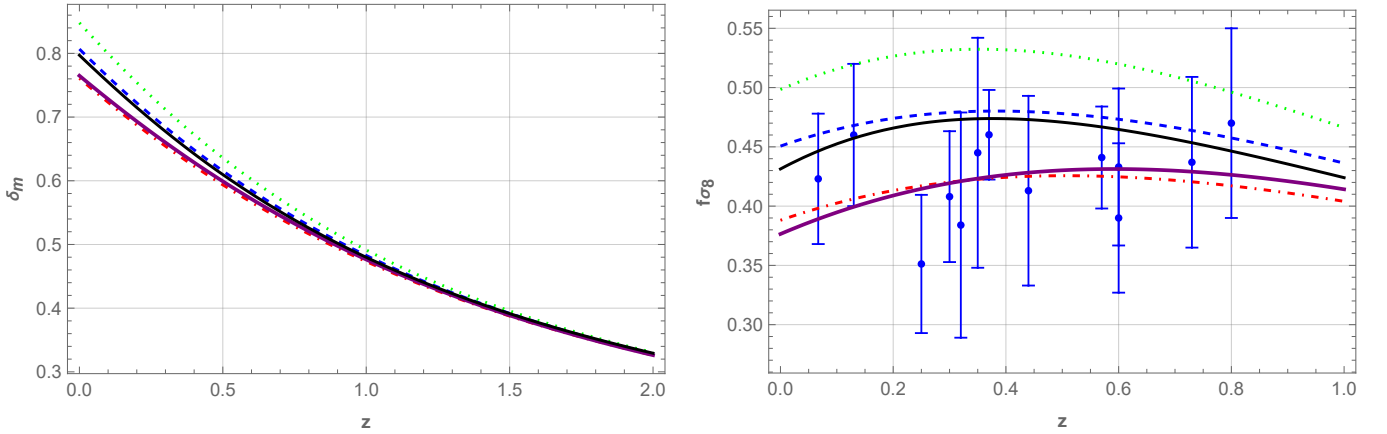
A. Numerical results

The theoretical curves for matter density perturbations are shown in Fig. 3a, based on various selections of model parameters. For our analysis, we observe that $\sigma(a) \sim \delta_m(a)$ while $\delta_m(a) \approx a = \frac{1}{1+z}$ [90, 93]. For the chosen model (30), from Fig. 3a, we determine the subsequent values: $\sigma_8 = 0.81$ (blue-dashed line), $\sigma_8 = 0.76$ (red-dot dashed line), $\sigma_8 = 0.85$ (green-dotted line), $\sigma_8 = 0.76$ (purple-thick line). For the Λ CDM model, we determine that $\sigma_8 = 0.8$ (black-thinning). These values serve as a good approximation that aligns with the findings shown in Refs.[15, 93–95].

In Fig. 3b, we illustrate the theoretical curves for the weighted linear growth rate $f\sigma_8(z)$ corresponding to various selections of model parameters. We notice that for the red-dot dashed line and the purple-thick line, the values of $f\sigma_8(z)$ are lower than the related standard from the Λ CDM model (black-thinning), suggesting that our model might reduce the σ_8 -tension. For the selected model (30), we extract the following values from Fig. 3b: $f\sigma_8(0) \approx 0.45$ (blue-dashed line), $f\sigma_8(0) \approx 0.39$ (red-dot dashed line), $f\sigma_8(0) \approx 0.50$ (green-dotted line), and $f\sigma_8(0) \approx 0.38$ (purple-thick line). In the case of the Λ CDM model, we find that $f\sigma_8(0) \approx 0.43$ (black-thinning line). To measure this impact, we establish the precise relative difference [91] as,

$$\Delta f\sigma_8(z) \equiv 100 \times \frac{f\sigma_8(z)_{\text{model}} - f\sigma_8(z)_{\Lambda\text{CDM}}}{f\sigma_8(z)_{\Lambda\text{CDM}}}, \quad (39)$$

In Fig. 3b, the red-dot dashed line represents $f\sigma_8(0) \approx 0.39$, whereas for the Λ CDM model, we calculate $f\sigma_8(0) \approx 0.43$, resulting in a relative difference of $\Delta f\sigma_8(0) \approx 9\%$. The purple-thick line indicates that the relative difference with the Λ CDM model is $\Delta f\sigma_8(0) \approx 11\%$. Consequently, the projection indicated by the red-dot dashed line is approximately 9% below the Λ CDM model prediction. The purple-thick line shows a deviation of roughly 11% below the Λ CDM model. This result represents an improvement over the findings associated with the XCDM parametrization, as reported in Ref. [91].



a) The graph displays the evolution of the matter density fluctuation, referred to as δ_m , to the redshift z across various dataset values, along with the corresponding evolution for the Λ CDM model.

b) The graph displays the evolution of the weighted growth rate $f\sigma_8$ and the related progression for the Λ CDM model. In this figure, we have used the complete redshift-space distortion (RSD) $f\sigma_8$ dataset listed in Table II of Ref. [93].

Figure 3: Evolution of the matter density perturbation δ_m and weighted growth rate $f\sigma_8$ with respect to redshift z using the relation $a = \frac{1}{1+z}$. In this graph, the blue-dashed line represents dataset CC+PN⁺, the red-dot dashed line corresponds to dataset CC+PN⁺+BAO, the green-dotted line represents dataset CC+PN⁺&SH0ES, the purple-thick line corresponds to dataset CC+PN⁺&SH0ES+BAO and black-thinning line corresponds to Λ CDM model.

VI. DYNAMICS OF COSMOLOGICAL PARAMETERS

In this section, we will examine the background cosmological parameters to investigate the behavior at the late time for the $f(T, \mathcal{T})$ model. Additionally, we will juxtapose these results with those from the standard Λ CDM

model. Fig. 4, displays the behavior of the Hubble parameter and comparative analysis of the evolution of the Hubble parameter between the selected model and the Λ CDM model for the PN^+ and the PN^+ & SH0ES data set combinations. It has been noted that the curves follow a similar pattern to that of the Λ CDM and remain well within the error margins. The analysis of these figures indicates that the model exhibits behavior consistent with that of the Λ CDM paradigm across the specified combination of data sets. We present the relative difference to demonstrate the differences between the selected and standard Λ CDM models.

$$\Delta_r H(z) = \frac{|H_{\text{model}} - H_{\Lambda\text{CDM}}|}{H_{\Lambda\text{CDM}}}. \quad (40)$$

Additionally, Fig. 5 showcase the evolution of the Hubble parameter and comparative analysis of the evolution of the Hubble parameter between the selected model and the Λ CDM model for various data sets, including the CC, PN^+ , PN^+ & SH0ES and BAO, with the incorporation of H_0 priors.

In Figs. 6, we illustrate the evolution of the distance modulus and comparative analysis of the evolution of the distance modulus function between the selected model and the Λ CDM model. For the selected cosmological model in comparison with the Λ CDM framework, utilizing a data set comprising 1701 data points from the SNIa observations. The analysis reveals a noteworthy concordance between the selected and Λ CDM models. The calculated relative difference can be defined as

$$\Delta_r \mu(z) = \frac{|\mu_{\text{model}} - \mu_{\Lambda\text{CDM}}|}{\mu_{\Lambda\text{CDM}}}. \quad (41)$$

Fig. 7 illustrates the progression of the distance modulus function alongside the relative difference in distance modulus for the CC, PN^+ , PN^+ & SH0ES and BAO data set, taking into account the H_0 priors. This observed trend is consistent with the patterns seen in Figs. 6, highlighting similar behaviors across the different datasets.

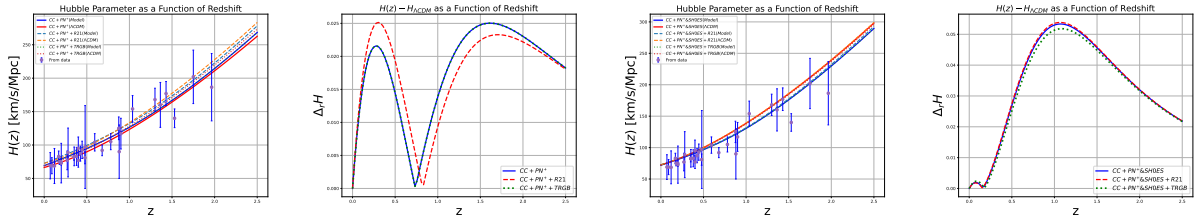


Figure 4: Evolutionary behavior of Hubble parameter and comparative analysis of the evolution of the Hubble parameter between the selected model and the Λ CDM model in redshift for the data set combination: CC, PN^+ (without SH0ES) and PN^+ & SH0ES (with SH0ES). The H_0 priors are: R21 and TRGB.

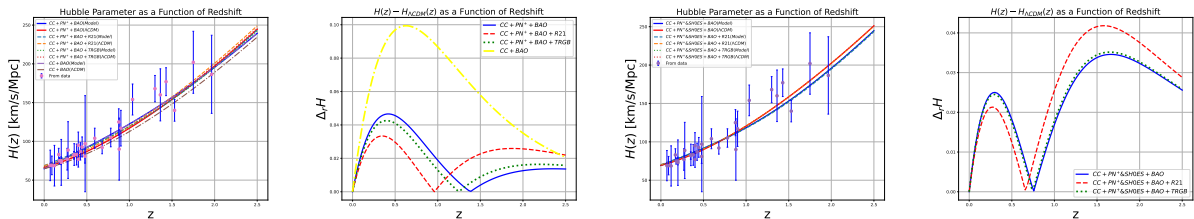


Figure 5: Evolutionary behavior of Hubble parameter and comparative analysis of the evolution of the Hubble parameter between the selected model and the Λ CDM model in redshift for the data sets combination: CC, PN^+ (without SH0ES), PN^+ & SH0ES (with SH0ES) and BAO. The H_0 priors are: R21 and TRGB.

The deceleration parameter, the total EoS and the matter-energy density as a function of redshift can be expressed

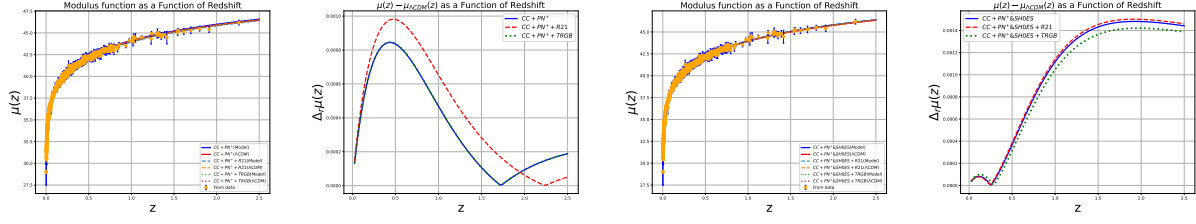


Figure 6: Evolutionary behavior of distance modulus and comparative analysis of the evolution of the distance modulus function between the selected model and the Λ CDM model in redshift for the datasets combination: CC, PN^+ (without SH0ES) and PN^+ &SH0ES (with SH0ES). The H_0 priors are: R21 and TRGB.

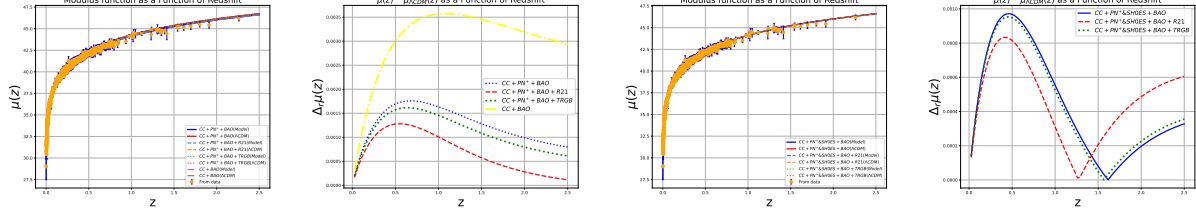


Figure 7: Evolutionary behavior of distance modulus and comparative analysis of the evolution of the distance modulus function between the selected model and the Λ CDM model in redshift for the data sets combination: CC, PN^+ (without SH0ES), PN^+ &SH0ES (with SH0ES) and BAO. The H_0 priors are: R21 and TRGB.

as,

$$q = -1 + \frac{(1+z)H'(z)}{H(z)}, \quad (42)$$

$$\omega_{\text{tot}} = -1 + \frac{2(1+z)H'(z)}{3H(z)}, \quad (43)$$

$$\Omega_m = \frac{\Omega_{m0}(1+z)^3 H_0^2}{H^2(z)}. \quad (44)$$

In Figs.-8, we illustrate the evolution of the deceleration parameter for both the selected model and the Λ CDM model. The selected model indicates a transition from a decelerating period to an accelerating phase of the Universe, implying its potential to represent the accelerated expansion of the Universe. Additionally, we determine the current value of the deceleration parameter. Details regarding the current value of the deceleration parameter and the transition point for various data set combinations can be found in Table V. The outcomes from the selected model concerning the current deceleration parameter value and the transition point are consistent with cosmological observations [96, 97]. In Figs. 9, we depict the evolution of the total EoS parameter for the selected model in comparison

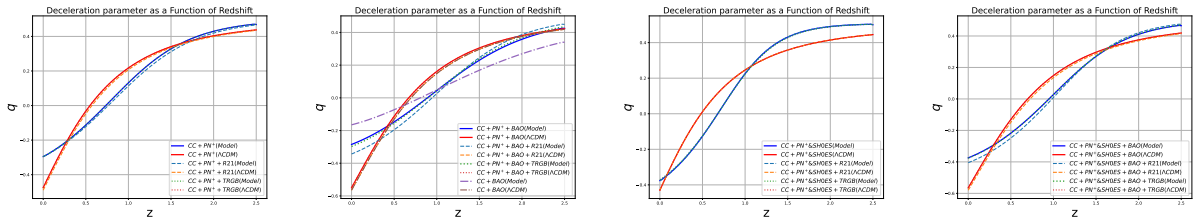


Figure 8: Evolutionary behavior of the deceleration parameter and Λ CDM model in redshift for the data sets combination: CC, PN^+ (without SH0ES), PN^+ &SH0ES (with SH0ES) and BAO. The H_0 priors are: R21 and TRGB.

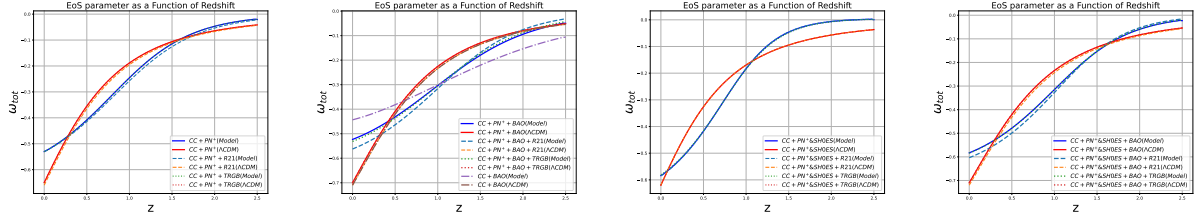


Figure 9: Evolutionary behavior of the EoS parameter and Λ CDM model in redshift for the data sets combination: CC, PN^+ (without SH0ES), PN^+ &SH0ES (with SH0ES) and BAO. The H_0 priors are: R21 and TRGB.

with the Λ CDM model. The EoS parameter indicates that our chosen model shows the quintessence phase of the Universe, as it satisfies the quintessence criterion where $-1 < \omega_{tot} < -\frac{1}{3}$. A comprehensive summary of the current values of the total EoS parameter is provided in Table V. In Figs. 10, we present the evolution of the density para-

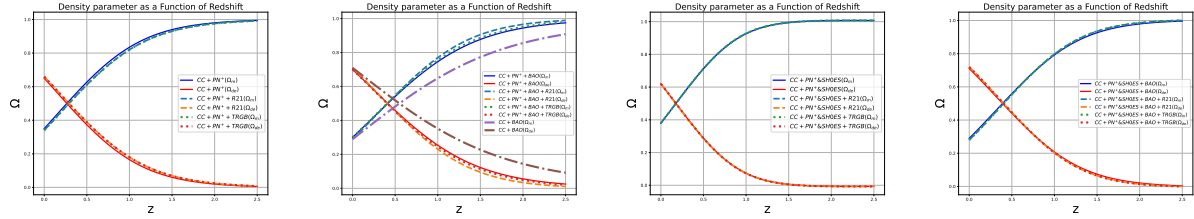


Figure 10: Evolutionary behavior of the density parameters and Λ CDM model in redshift for the data sets combination: CC, PN^+ (without SH0ES), PN^+ &SH0ES (with SH0ES) and BAO. The H_0 priors are: R21 and TRGB.

eters for both matter and DE in the Universe as redshift varies. These plots demonstrate the shifting interaction between matter and DE, showing that the density of DE increasingly dominates in later epochs, showing the accelerated expansion. The current values of these density parameters are listed in Table V. During the early stages of the Universe, DM constitutes the main part of the energy density at higher redshifts, far outpacing DE. As redshift decreases, the proportion of DM drops while the influence of DE steadily rises. In the later stages of the Universe, DE becomes the leading component and at lower redshifts, it overtakes DM, driving the accelerated expansion.

The $Om(z)$ diagnostic serves as an alternative method to distinguish between various DE cosmological models. This can be represented as [98, 99].

$$Om(z) = \frac{E^2(z) - 1}{(1+z)^3 - 1}. \quad (45)$$

Assessing the $Om(z)$ values across different redshifts can yield insights into the characteristics and dynamics of DE. The procedure for two-point difference diagnostics can be described as follows:

$$Om(z_1 - z_2) = Om(z_1) - Om(z_2). \quad (46)$$

If $Om(z_1, z_2) > 0$, this suggests the model represents a quintessence scenario, while $Om(z_1, z_2) < 0$ implies it exhibits phantom behavior, given that $z_1 < z_2$. Additionally, if $Om(z)$ remains consistent across various redshifts, it indicates a potential connection between DE and the cosmological constant [98]. We have compared the model discussed here with the Λ CDM model, as shown in Fig. 11. The $Om(z)$ parameter displays stability within the redshift range $0 < z < 2.5$. This stability is crucial for understanding the dynamics of the Universe and its accelerated expansion. The slope of $Om(z)$ is an important indicator for DE models. A positive slope suggests the presence of phantom behavior, which is characterized by an EoS $\omega < -1$. Conversely, a negative slope is linked to the quintessence region, where $\omega > -1$. In Fig. 11, the slope of the $Om(z)$ parameter shows a downward trend as redshift increases, suggesting that the impact of DE becomes more significant over time. This reduction indicates a transformation in the dynamics of the Universe, illustrating the evolving roles of matter and DE as the Universe

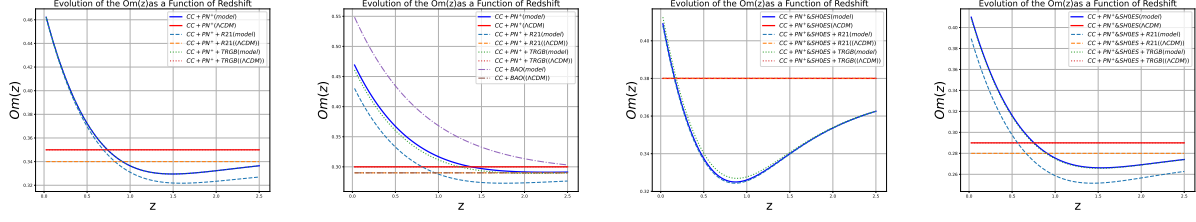


Figure 11: Evolutionary behavior of the $Om(z)$ parameter and Λ CDM model in redshift for the data sets combination: CC, PN^+ (without SH0ES), PN^+ &SH0ES (with SH0ES) and BAO. The H_0 priors are: R21 and TRGB.

progresses. This decline is consistent with the quintessence phase of the Universe, where the EoS ω is greater than -1 .

The whisker plot represents the ranges and central tendencies of the model parameters. In Fig. 12, the whisker plot effectively distinguishes parameter values derived from different combinations of data sets. Through Fig. 12, we observe a notable contrast in the values of the parameters (H_0 , Ω_{m0} , n) between the PN^+ (without SH0ES) and PN^+ & SH0ES data set combinations. Across all combinations of data sets, we find a lower value of H_0 in the CC+BAO data set combination where both PN^+ and PN^+ & SH0ES are absent. Additionally, we can observe how the inclusion of H_0 priors influences the values of H_0 within the PN^+ data set combination, as incorporating the H_0 priors increases the H_0 values.

Data set	For $f(T, \mathcal{T})$ model					For the Λ CDM model		
	q_0	ω_0	z_{tr}	Ω_m^0	Ω_{de}^0	q_0	ω_0	z_{tr}
CC+ PN^+	-0.29	-0.53	0.73	0.35	0.65	-0.48	-0.65	0.53
CC+ PN^+ +R21	-0.30	-0.53	0.76	0.34	0.66	-0.49	-0.65	0.56
CC+ PN^+ +TRGB	-0.30	-0.53	0.73	0.35	0.65	-0.48	-0.65	0.53
CC+ PN^+ +BAO	-0.28	-0.52	0.88	0.3	0.7	-0.55	-0.70	0.66
CC+ PN^+ +BAO+R21	-0.34	-0.56	0.93	0.29	0.71	-0.57	-0.71	0.68
CC+ PN^+ +BAO+TRGB	-0.30	-0.53	0.88	0.3	0.7	-0.55	-0.7	0.66
CC+BAO	-0.17	-0.44	0.78	0.29	0.71	-0.565	-0.71	0.68
CC+ PN^+ &SH0ES	-0.37	-0.58	0.66	0.38	0.62	-0.43	-0.62	0.48
CC+ PN^+ &SH0ES+R21	-0.38	-0.58	0.66	0.38	0.62	-0.43	-0.62	0.48
CC+ PN^+ &SH0ES+TRGB	-0.37	-0.58	0.66	0.38	0.62	-0.43	-0.62	0.48
CC+ PN^+ &SH0ES+BAO	-0.37	-0.59	0.93	0.29	0.71	-0.565	-0.71	0.68
CC+ PN^+ &SH0ES+BAO+R21	-0.40	-0.60	0.96	0.28	0.72	-0.58	-0.72	0.71
CC+ PN^+ &SH0ES+BAO+TRGB	-0.37	-0.58	0.93	0.29	0.71	-0.57	-0.71	0.68

Table V: Present value of the parameters and the transition point. The upper or lower indices 0 represent the current time at $z = 0$.

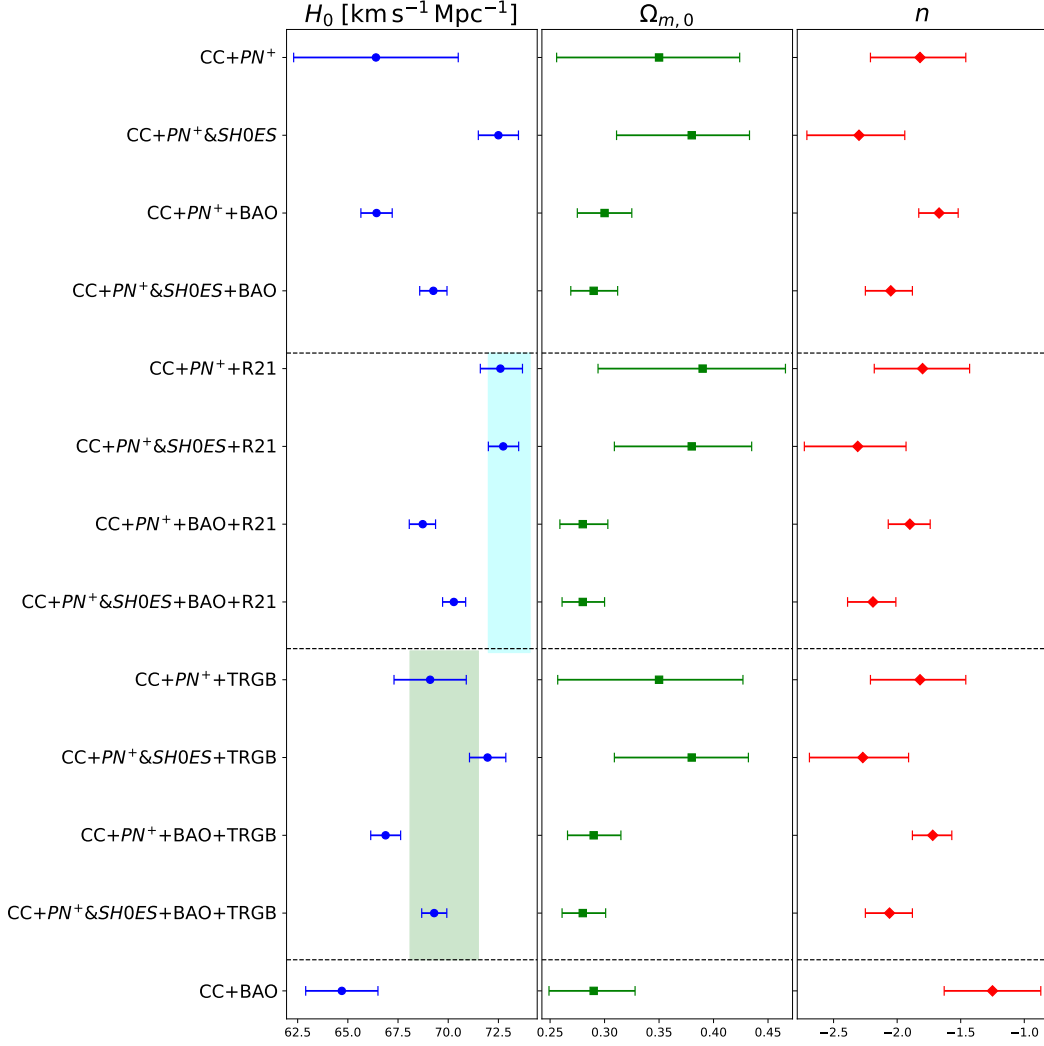


Figure 12: Whisker plot for the chosen $f(T, \mathcal{T})$ model. This plot provides a visual representation of the distributions of several key parameters: the Hubble constant H_0 , the matter-energy density Ω_{m0} and the model parameters n . In the first column, the cyan-shaded region represents the R21 prior, while the green-shaded region indicates the TRGB prior.

VII. CONCLUSION

In this study, we have presented cosmological model that supports late-time cosmic acceleration of the Universe in the framework of $f(T, \mathcal{T})$ gravity using various cosmological dataset combinations. Our analysis incorporates datasets including the CC, PN $^+$ (without SH0ES), PN $^+$ & SH0ES (with SH0ES) and BAO observations alongside the H_0 priors from R21 and TRGB. We specifically focus on a comparative analysis between the PN $^+$ (without SH0ES) and PN $^+$ & SH0ES (with SH0ES) datasets, alongside the BAO datasets and specific combinations of the H_0 priors. We present the whisker plot in Fig.-12 to emphasize the differences between these datasets. Additionally, the findings derived from the chosen model have been contrasted with those of the standard Λ CDM model. Our analysis aimed at obtaining the best-fit values of the model parameters using the CC, PN $^+$, PN $^+$ & SH0ES and BAO data sets alongside the H_0 priors R21 and TRGB.

In examining the PN $^+$ (without SH0ES) and PN $^+$ & SH0ES (with SH0ES) datasets, we have observed that the H_0 value is lower for the PN $^+$ (without SH0ES) dataset when compared to the PN $^+$ & SH0ES (with SH0ES) dataset. The increase in the H_0 value for the PN $^+$ & SH0ES (with SH0ES) dataset can be attributed to including the

SH0ES data points. The SH0ES points elevate the H_0 value. In Tables- I and III, the results for the PN^+ and PN^+ & SH0ES datasets are presented, respectively. Table-I shows a higher H_0 value for the dataset combination $\text{CC}+\text{PN}^++\text{R21}$ and a lower value for the $\text{CC}+\text{BAO}$ dataset combination. Consequently, the model yields a lower H_0 value without SNIa, SH0ES points and H_0 priors. Thus, we can conclude that incorporating the BAO dataset results in a decrease in H_0 values. In Table- III, the combination $\text{CC}+\text{PN}^++\text{SH0ES}+\text{R21}$ yields a higher H_0 value. The results from Tables- I and III suggest that the $\text{CC}+\text{PN}^++\text{SH0ES}+\text{R21}$ dataset combination leads to a higher H_0 value, whereas the BAO dataset combination results in a lower value. Our result indicates that the highest H_0 value for the $\text{CC}+\text{PN}^++\text{R21}$ aligns with the elevated H_0 value reported by the SH0ES team (R22), which is stated as $H_0 = 73.30 \pm 1.04 \text{ km s}^{-1} \text{ Mpc}^{-1}$ [12]. Meanwhile, the H_0 value from the BAO dataset inclusion is consistent with the Planck Collaboration, which reports a Hubble constant of $67.4 \pm 0.5 \text{ km s}^{-1} \text{ Mpc}^{-1}$ [15]. In contrast, Aboot et al. [16] present a value of $67.2_{-1.0}^{+1.2} \text{ km s}^{-1} \text{ Mpc}^{-1}$. The H_0 findings for PN^+ and PN^+ & SH0ES in our study resemble those obtained by Brout et al [56].

Our analysis of linear matter perturbations in $f(T, \mathcal{T})$ gravity demonstrates that the growth rate of matter overdensity is influenced by the effective Newton's constant G_{eff} , modifying the standard evolution of density fluctuations. The results indicate that the modified $f(T, \mathcal{T})$ model can help address the σ_8 tension by predicting a lower growth rate $f\sigma_8(0)$ compared to ΛCDM . Consequently, in Fig. 3b, the results indicated by the red-dot dashed line are approximately 9% below the ΛCDM model prediction. In contrast, the purple-thick line shows a deviation of roughly 11% below ΛCDM . These results indicate that the $f(T, \mathcal{T})$ model could provide a better fit to large-scale structure observations, potentially offering an alternative explanation for the discrepancies in cosmic growth measurements as compared to ΛCDM .

Alternatively, we delve deeper into our chosen $f(T, \mathcal{T})$ model, which exhibits fascinating characteristics due to its absence of a corresponding ΛCDM limit. In particular, this model has no combination of parameter values that can replicate the precise behavior of the ΛCDM model. From a statistical viewpoint, the AIC and BIC values for the data set combination $\text{CC}+\text{PAN}^+$ and $\text{CC}+\text{PAN}^++\text{SH0ES}$ are shown to be quite close to those of the conventional ΛCDM model, implying that this combination of data supports the ΛCDM model effectively. However, when the BAO data set is incorporated with $\text{CC}+\text{PAN}^+$ and $\text{CC}+\text{PAN}^++\text{SH0ES}$, both the ΔAIC and ΔBIC values rise. It suggests that the $\text{CC}+\text{PAN}^++\text{BAO}$ and $\text{CC}+\text{PAN}^++\text{SH0ES}+\text{BAO}$ data set combination does not provide compelling evidence in favor of the ΛCDM model.

To explore late-time cosmology, we demonstrate the evolution of background cosmological parameters, including the deceleration parameter, the total equation of state (EoS) parameter, the energy density parameters for both matter and dark energy, and the $Om(z)$ diagnostic parameter for our chosen $f(T, \mathcal{T})$ model in comparison to the standard ΛCDM model. The current values for the deceleration and EoS parameters, energy density, and the transition redshift from deceleration to acceleration are summarized in Table-V. The observed behavior of the deceleration parameter suggests that the selected model successfully captures the shift from deceleration in the early Universe to acceleration in later periods. The dynamics of the EoS parameter indicate a quintessence-like characteristic during the late-time phase of the evolution. The energy density parameters reveal a transition from an early Universe dominated by matter to a late-time phase predominantly governed by dark energy. Thus, the model can explain the late-time cosmic phenomena of the Universe.

In the future, this research could be combined with Cosmic Microwave Background (CMB) data, the level of scalar perturbations, and large-scale structure formation and evolution. We expect to gain a more profound insight into the dynamics of inflation and other significant events in the early Universe, which may offer a fresh approach to examining the essential characteristics of cosmic evolution.

VIII. APPENDIX

We present the results of the ΛCDM model highlighting the posterior distributions in Figs. 13 and 14. These figures include the 1σ and 2σ confidence intervals for various combinations of datasets, providing a comprehensive examination of parameter constraints. Detailed results for each dataset combination are summarized in Tables VI and VII. This methodology emphasizes the consistency of our findings with the standard predictions of the ΛCDM paradigm, facilitating a rigorous assessment on the performance of the model across the selected datasets.

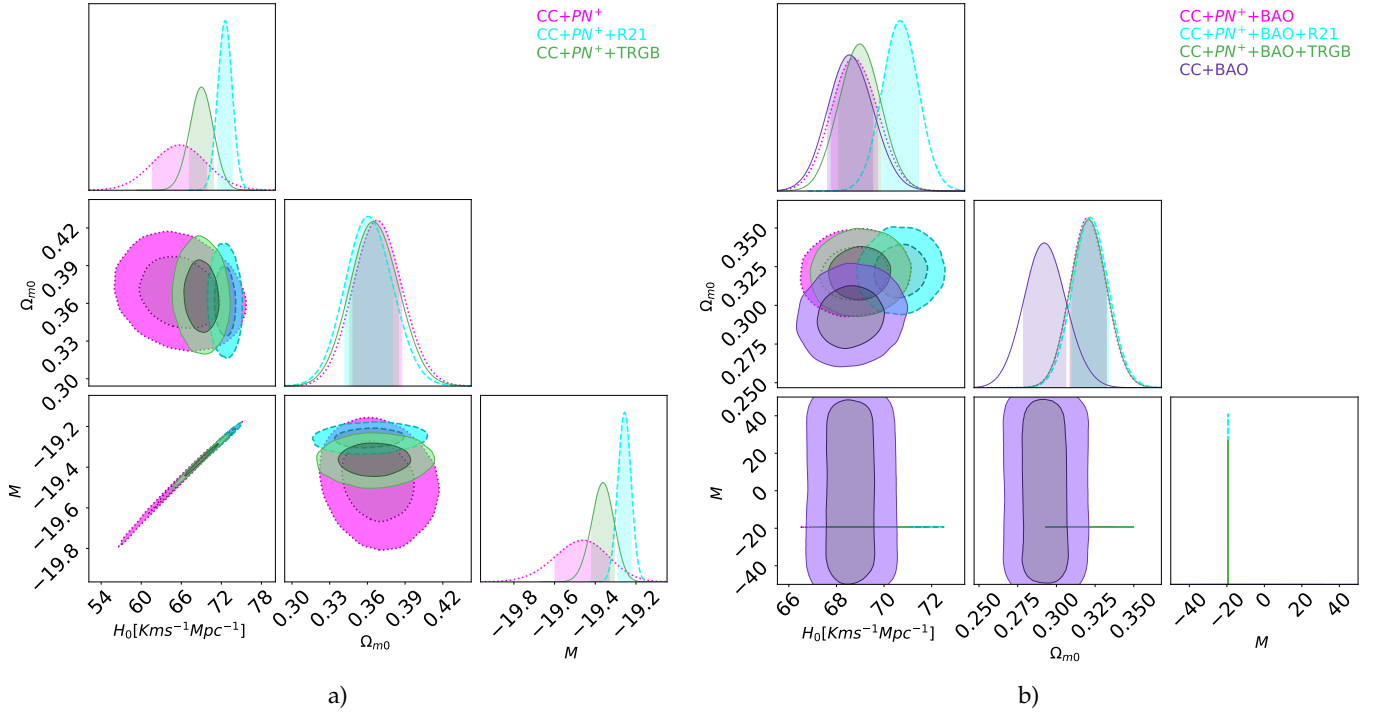


Figure 13: The contour plot of 1σ and 2σ uncertainty regions and posterior distribution for the model parameters with the combination of data sets (a) CC, PN^+ (b) CC, PN^+ and BAO. The H_0 priors are: TRGB (Green) and R21 (Cyan).

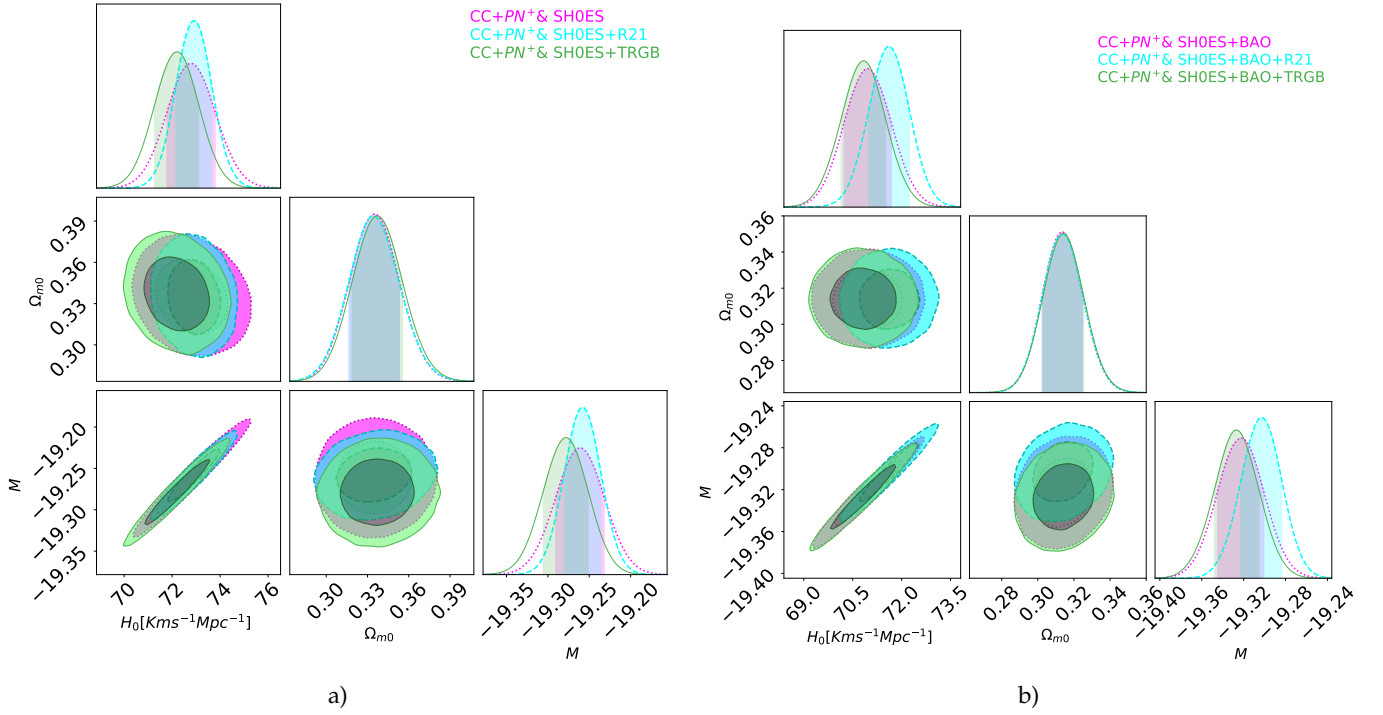


Figure 14: The contour plot of 1σ and 2σ uncertainty regions and posterior distribution for the model parameters with the combination of data sets (a) CC, PN^+ & SH0ES (b) CC, PN^+ & SH0ES and BAO. The H_0 priors are: TRGB (Green) and R21 (Cyan).

Table VI: The results for the Λ CDM model. The first column identifies the data set combinations and the applied H_0 priors. The second and third columns present the derived values for H_0 and $\Omega_{m,0}$ respectively, while the fourth column displays the value of the nuisance parameter. The fifth column provides the minimized χ^2_{min} values, with the sixth and seventh columns showing the AIC and BIC values respectively. **(Without SH0ES data points)**

Λ CDM	H_0	$\Omega_{m,0}$	M	χ^2_{min}	AIC	BIC
CC+PN ⁺	65.7 ± 4.1	$0.368^{+0.019}_{-0.020}$	$-19.46^{+0.13}_{-0.14}$	1792.30	1798.30	1802.02
CC+PN ⁺ +R21	$72.6^{+1.0}_{-1.1}$	0.361 ± 0.019	$-19.256^{+0.032}_{-0.033}$	1795.64	1801.64	1805.35
CC+PN ⁺ +TRGB	$69.0^{+1.8}_{-1.7}$	$0.365^{+0.020}_{-0.019}$	$-19.362^{+0.055}_{-0.057}$	1793.20	1799.20	1802.92
CC+PN ⁺ +BAO	$68.73^{+1.00}_{-0.95}$	$0.320^{+0.012}_{-0.011}$	$-19.387^{+0.033}_{-0.030}$	1817.75	1823.75	1827.36
CC+PN ⁺ +BAO+R21	$70.68^{+0.76}_{-0.75}$	$0.322^{+0.012}_{-0.011}$	-19.326 ± 0.024	1827.16	1833.16	1836.78
CC+PN ⁺ +BAO+TRGB	$68.99^{+0.88}_{-0.90}$	$0.321^{+0.011}_{-0.012}$	-19.379 ± 0.029	1818.00	1824.00	1827.61
CC+BAO	$68.56^{+0.97}_{-0.93}$	$0.292^{+0.014}_{-0.013}$	-	20.14	26.14	29.76

Table VII: The results for the Λ CDM model. The first column identifies the data set combinations and the applied H_0 priors. The second and third columns present the derived values for H_0 and $\Omega_{m,0}$ respectively, while the fourth column displays the value of the nuisance parameter. The fifth column provides the minimized χ^2_{min} values, with the sixth and seventh columns showing the AIC and BIC values respectively. **(With SH0ES data points)**

Λ CDM	H_0	$\Omega_{m,0}$	M	χ^2_{min}	AIC	BIC
CC+PN ⁺ & SH0ES	72.8 ± 1.0	0.335 ± 0.018	$-19.261^{+0.029}_{-0.030}$	1539.22	1545.22	1548.93
CC+PN ⁺ & SH0ES+R21	72.91 ± 0.75	$0.334^{+0.019}_{-0.018}$	-19.258 ± 0.022	1539.25	1545.25	1548.96
CC+PN ⁺ & SH0ES+TRGB	$72.22^{+0.89}_{-0.95}$	$0.337^{+0.019}_{-0.018}$	-19.278 ± 0.027	1541.18	1547.18	1550.89
CC+PN ⁺ & SH0ES+BAO	$70.95^{+0.74}_{-0.71}$	0.313 ± 0.011	$-19.322^{+0.021}_{-0.023}$	1567.17	1573.17	1576.90
CC+PN ⁺ & SH0ES+BAO+R21	$71.60^{+0.64}_{-0.61}$	0.314 ± 0.011	$-19.303^{+0.019}_{-0.020}$	1569.96	1575.96	1579.67
CC+PN ⁺ & SH0ES+BAO+TRGB	$70.82^{+0.69}_{-0.68}$	$0.315^{+0.011}_{-0.012}$	$-19.327^{+0.022}_{-0.021}$	1567.50	1573.50	1577.23

ACKNOWLEDGEMENTS

LKD acknowledges the financial support provided by University Grants Commission (UGC) through Senior Research Fellowship UGC Ref. No.: 191620180688 to carry out the research work. BM acknowledges the support of Anusandhan National Research Foundation(ANRF), Science & Engineering Research Board(SERB), DST for the grant (File No: CRG/2023/000475). The authors gratefully acknowledge the computing time provided on the high-performance computing facility, Sharanga, at the Birla Institute of Technology and Science - Pilani, Hyderabad Campus.

IX. REFERENCES

-
- [1] **Supernova Search Team** Collaboration, A. G. Riess *et al.*, “Observational evidence from supernovae for an accelerating universe and a cosmological constant,” *Astron. J.* **116** (1998) 1009–1038, [arXiv:astro-ph/9805201](#).

- [2] **Supernova Cosmology Project** Collaboration, S. Perlmutter *et al.*, “Measurements of Ω and Λ from 42 high redshift supernovae,” *Astrophys. J.* **517** (1999) 565–586, [arXiv:astro-ph/9812133](#).
- [3] C. L. Bennett *et al.*, “First-Year Wilkinson Microwave Anisotropy Probe (WMAP)* Observations: Preliminary Maps and Basic Results,” *The Astrophysical Journal Supplement Series* **148** (2003) no. 1, 1, [arXiv:astro-ph/0302207](#).
- [4] M. Tegmark *et al.*, “Cosmological parameters from SDSS and WMAP,” *Physical Review D* **69** (2004) no. 10, , [arXiv:astro-ph/0310723](#).
- [5] S. Alam *et al.*, “The clustering of galaxies in the completed SDSS-III Baryon Oscillation Spectroscopic Survey: cosmological analysis of the DR12 galaxy sample,” *Monthly Notices of the Royal Astronomical Society* **470** (2017) no. 3, 2617–2652, [arXiv:1607.03155 \[astro-ph.CO\]](#).
- [6] D. M. Scolnic *et al.*, “The Complete Light-curve Sample of Spectroscopically Confirmed SNe Ia from Pan-STARRS1 and Cosmological Constraints from the Combined Pantheon Sample,” *The Astrophysical Journal* **859** (2018) no. 2, 101, [arXiv:1710.00845 \[astro-ph.CO\]](#).
- [7] A. G. Riess *et al.*, “Large Magellanic Cloud Cepheid Standards Provide a 1% Foundation for the Determination of the Hubble Constant and Stronger Evidence for Physics beyond Λ CDM,” *Astrophys. J.* **876** (2019) no. 1, 85, [arXiv:1903.07603 \[astro-ph.CO\]](#).
- [8] D. Benisty and D. Staicova, “Testing late-time cosmic acceleration with uncorrelated baryon acoustic oscillation dataset,” *Astronomy & Astrophysics* **647** (2021) A38, [arXiv:2009.10701 \[astro-ph.CO\]](#).
- [9] **DES Collaboration** Collaboration, “Dark Energy Survey Year 3 results: calibration of lens sample redshift distributions using clustering redshifts with BOSS/eBOSS,” *Monthly Notices of the Royal Astronomical Society* **513** (2022) no. 4, 5517–5539, [arXiv:2012.12826 \[astro-ph.CO\]](#). <http://dx.doi.org/10.1093/mnras/stac1160>.
- [10] R. P. Gupta, “JWST early Universe observations and Λ CDM cosmology,” *Monthly Notices of the Royal Astronomical Society* **524** (2023) no. 3, 3385–3395, [arXiv:2309.13100 \[astro-ph.CO\]](#).
- [11] **Planck Collaboration** Collaboration, “Planck2013 results. XVI. Cosmological parameters,” *Astronomy & Astrophysics* **571** (2014) A16, [arXiv:1303.5076 \[astro-ph.CO\]](#).
- [12] A. G. Riess *et al.*, “A Comprehensive Measurement of the Local Value of the Hubble Constant with 1 km s^{−1} Mpc^{−1} Uncertainty from the Hubble Space Telescope and the SH0ES Team,” *The Astrophysical Journal Letters* **934** (2022) no. 1, L7, [arXiv:2112.04510 \[astro-ph.CO\]](#).
- [13] Wang *et al.*, “H0LICOW XIII. A 2.4 % measurement of H_0 from lensed quasars: 5.3 σ tension between early and late-Universe probes,” *Monthly Notices of the Royal Astronomical Society* **498** (2019) no. 1, 1420–1439, [arXiv:1907.04869 \[astro-ph.CO\]](#).
- [14] W. L. Freedman *et al.*, “The Carnegie-Chicago Hubble Program. VIII. An Independent Determination of the Hubble Constant Based on the Tip of the Red Giant Branch*,” *The Astrophysical Journal* **882** (2019) no. 1, 34, [arXiv:1907.05922 \[astro-ph.CO\]](#).
- [15] **Planck** Collaboration, N. Aghanim *et al.*, “Planck 2018 results. VI. Cosmological parameters,” *Astron. Astrophys.* **641** (2020) A6, [arXiv:1807.06209 \[astro-ph.CO\]](#). [Erratum: *Astron. Astrophys.* 652, C4 (2021)].
- [16] **DES Collaboration** Collaboration, “Dark Energy Survey Year 1 Results: A Precise H_0 Estimate from DES Y1, BAO, and D/H Data,” *Monthly Notices of the Royal Astronomical Society* **480** (2018) no. 3, 3879–3888, [arXiv:1711.00403 \[astro-ph.CO\]](#).
- [17] E. Di Valentino, A. Melchiorri, and O. Mena, “Can interacting dark energy solve the H_0 tension?,” *Physical Review D* **96** (2017) no. 4, , [arXiv:1704.08342 \[astro-ph.CO\]](#).
- [18] E. Di Valentino *et al.*, “In the realm of the Hubble tension - a review of solutions,” *Classical and Quantum Gravity* **38** (2021) no. 15, 153001, [arXiv:2103.01183 \[astro-ph.CO\]](#).
- [19] M. Ata *et al.*, “The clustering of the SDSS-IV extended Baryon Oscillation Spectroscopic Survey DR14 quasar sample: first measurement of baryon acoustic oscillations between redshift 0.8 and 2.2,” *Mon. Not. Roy. Astron. Soc.* **473** (2017) no. 4, 4773–4794, [arXiv:1705.06373 \[astro-ph.CO\]](#).
- [20] M. Asgari *et al.*, “KiDS-1000 cosmology: Cosmic shear constraints and comparison between two point statistics,” *Astronomy & Astrophysics* **645** (2021) A104, [arXiv:2007.15633 \[astro-ph.CO\]](#).
- [21] J. Ruiz-Zapatero *et al.*, “Geometry versus growth: Internal consistency of the flat Λ CDM model with KiDS-1000,” *Astronomy & Astrophysics* **655** (2021) A11, [arXiv:2105.09545 \[astro-ph.CO\]](#).
- [22] V. Ghirardini *et al.*, “The SRG/eROSITA all-sky survey: Cosmology constraints from cluster abundances in the western Galactic hemisphere,” *Astronomy & Astrophysics* **689** (2024) A298, [arXiv:2402.08458 \[astro-ph.CO\]](#).
- [23] S. Nojiri and S. D. Odintsov, “Modified $f(R)$ gravity consistent with realistic cosmology: From a matter dominated epoch to a dark energy universe,” *Phys. Rev. D* **74** (2006) 086005, [arXiv:hep-th/0608008](#).
- [24] S. Nojiri and S. D. Odintsov, “Unifying inflation with Λ CDM epoch in modified $f(R)$ gravity consistent with Solar System Test,” *Physics Letters B* **657** (2007) no. 4, 238–245, [arXiv:0707.1941 \[hep-th\]](#).
- [25] T. P. Sotiriou and V. Faraoni, “ $f(R)$ Theories Of Gravity,” *Rev. Mod. Phys.* **82** (2010) 451–497, [arXiv:0805.1726 \[gr-qc\]](#).

- [26] S. Capozziello and M. De Laurentis, “Extended Theories of Gravity,” *Phys. Rept.* **509** (2011) 167–321, [arXiv:1108.6266 \[gr-qc\]](#).
- [27] J. W. Maluf, “Hamiltonian formulation of the teleparallel description of general relativity,” *J. Math. Phys.* **35** (1994) 335–343, [arXiv:gr-qc/0002059](#).
- [28] R. Aldrovandi and J. G. Pereira, *Teleparallel Gravity: An Introduction*. Springer, 2013.
- [29] R. Weitzenböck, ‘*Invariantentheorie*’. Noordhoff, Gronningen, 1923.
- [30] G. R. Bengochea and R. Ferraro, “Dark torsion as the cosmic speed-up,” *Phys. Rev. D* **79** (2009) 124019, [arXiv:0812.1205 \[astro-ph\]](#).
- [31] R. Ferraro and F. Fiorini, “On Born-Infeld Gravity in Weitzenböck spacetime,” *Phys. Rev. D* **78** (2008) 124019, [arXiv:0812.1981 \[gr-qc\]](#).
- [32] E. V. Linder, “Einstein’s Other Gravity and the Acceleration of the Universe,” *Phys. Rev. D* **81** (2010) 127301, [arXiv:1005.3039 \[astro-ph.CO\]](#). [Erratum: *Phys. Rev. D* **82**, 109902 (2010)].
- [33] S.-H. Chen *et al.*, “Cosmological perturbations in $f(T)$ gravity,” *Phys. Rev. D* **83** (2011) 023508, [arXiv:1008.1250 \[astro-ph.CO\]](#).
- [34] Y.-F. Cai *et al.*, “ $f(T)$ teleparallel gravity and cosmology,” *Reports on Progress in Physics* **79** (2016) no. 10, 106901.
- [35] L. K. Duchaniya *et al.*, “Dynamical stability analysis of accelerating $f(T)$ gravity models,” *Eur. Phys. J. C* **82** (2022) no. 5, 448, [arXiv:2202.08150 \[gr-qc\]](#).
- [36] R. Briffa *et al.*, “Growth of structures using redshift space distortion in $f(T)$ cosmology,” *Monthly Notices of the Royal Astronomical Society* **528** (2024) no. 2, 2711–2727, [arXiv:2310.09159 \[gr-qc\]](#).
- [37] L. K. Duchaniya, K. Gandhi, and B. Mishra, “Attractor behavior of $f(T)$ modified gravity and the cosmic acceleration,” *Physics of the Dark Universe* **44** (2024) 101461, [arXiv:2303.09076 \[gr-qc\]](#).
- [38] G. Kofinas and E. N. Saridakis, “Teleparallel equivalent of Gauss-Bonnet gravity and its modifications,” *Phys. Rev. D* **90** (2014) 084044, [arXiv:1404.2249 \[gr-qc\]](#).
- [39] G. Kofinas and E. N. Saridakis, “Cosmological applications of $F(T, T_G)$ gravity,” *Phys. Rev. D* **90** (2014) 084045, [arXiv:1408.0107 \[gr-qc\]](#).
- [40] C. Escamilla-Rivera and J. Levi Said, “Cosmological viable models in $f(T, B)$ theory as solutions to the H_0 tension,” *Class. Quant. Grav.* **37** (2020) no. 16, 165002, [arXiv:1909.10328 \[gr-qc\]](#).
- [41] S. A. Kadam, N. P. Thakkar, and B. Mishra, “Dynamical system analysis in teleparallel gravity with boundary term,” *The European Physical Journal C* **83** (2023) no. 9, , [arXiv:2306.06677 \[gr-qc\]](#).
- [42] M. Gonzalez-Espinoza and G. Otalora, “Cosmological dynamics of dark energy in scalar-torsion $f(T, \phi)$ gravity,” *Eur. Phys. J. C* **81** (2021) no. 5, 480, [arXiv:2011.08377 \[gr-qc\]](#).
- [43] M. Gonzalez-Espinoza, G. Otalora, and J. Saavedra, “Stability of scalar perturbations in scalar-torsion $f(T, \phi)$ gravity theories in the presence of a matter fluid,” *JCAP* **10** (2021) 007, [arXiv:2101.09123 \[gr-qc\]](#).
- [44] L. K. Duchaniya, B. Mishra, and J. L. Said, “Noether symmetry approach in scalar-torsion $f(T, \phi)$ gravity,” *The European Physical Journal C* **83** (2023) no. 7, , [arXiv:2210.11944 \[gr-qc\]](#).
- [45] L. K. Duchaniya *et al.*, “Dynamical systems analysis in $f(T, \phi)$ gravity,” *The European Physical Journal C* **83** (2023) no. 1, , [arXiv:2209.03414 \[gr-qc\]](#).
- [46] T. Harko *et al.*, “ $f(T, T)$ gravity and cosmology,” *Journal of Cosmology and Astroparticle Physics* **2014** (2014) no. 12, 021, [arXiv:1405.0519 \[gr-qc\]](#).
- [47] D. Momeni and R. Myrzakulov, “Cosmological reconstruction of $f(T, T)$ gravity,” *International Journal of Geometric Methods in Modern Physics* **11** (2014) no. 08, 1450077, [arXiv:1405.5863 \[gr-qc\]](#).
- [48] G. Farrugia and J. L. Said, “Growth factor in $f(T, T)$ gravity,” *Phys. Rev. D* **94** (2016) 124004, [arXiv:1612.00974 \[gr-qc\]](#).
- [49] E. L. B. Junior *et al.*, “Reconstruction, thermodynamics and stability of the Λ CDM model in $f(T, T)$ gravity,” *Classical and Quantum Gravity* **33** (2016) no. 12, 125006, [arXiv:1501.00621 \[gr-qc\]](#).
- [50] M. Pace and J. L. Said, “Quark Stars in $f(T, T)$ -Gravity,” *The European Physical Journal C* **77** (2017) no. 2, , [arXiv:1701.04761 \[gr-qc\]](#).
- [51] L. K. Duchaniya, S. V. Lohakare, and B. Mishra, “Cosmological models in $f(T, T)$ gravity and the dynamical system analysis,” *Physics of the Dark Universe* **43** (2024) 101402, [arXiv:2302.07132 \[gr-qc\]](#).
- [52] S. Vagnozzi, “New physics in light of the H_0 tension: An alternative view,” *Physical Review D* **102** (2020) no. 2, 023518, [arXiv:1907.07569 \[astro-ph.CO\]](#).
- [53] W. L. Freedman, “Measurements of the hubble constant: Tensions in perspective,” *The Astrophysical Journal* **919** (2021) no. 1, 16, [arXiv:2106.15656 \[astro-ph\]](#). <http://dx.doi.org/10.3847/1538-4357/ac0e95>.
- [54] E. Abdalla *et al.*, “Cosmology intertwined: A review of the particle physics, astrophysics, and cosmology associated with the cosmological tensions and anomalies,” *Journal of High Energy Astrophysics* **34** (2022) 49–211, [arXiv:2203.06142 \[astro-ph.CO\]](#).

- [55] M. Moresco *et al.*, “Unveiling the universe with emerging cosmological probes,” *Living Reviews in Relativity* **25** (2022) no. 1, , [arXiv:2201.07241 \[astro-ph.CO\]](#).
- [56] D. Brout *et al.*, “The Pantheon+ Analysis: Cosmological Constraints,” *The Astrophysical Journal* **938** (2022) no. 2, 110, [arXiv:2202.04077 \[astro-ph.CO\]](#).
- [57] R. Briffa *et al.*, “Impact of H_0 priors on $f(T)$ late time cosmology,” *The European Physical Journal Plus* **137** (2022) no. 5, , [arXiv:2108.03853 \[astro-ph.CO\]](#).
- [58] S. Vagnozzi, “Seven Hints That Early-Time New Physics Alone Is Not Sufficient to Solve the Hubble Tension,” *Universe* **9** (2023) no. 9, 393, [arXiv:2308.16628 \[astro-ph.CO\]](#).
- [59] R. Briffa *et al.*, “Constraints on $f(T)$ cosmology with Pantheon+,” *Monthly Notices of the Royal Astronomical Society* **522** (2023) no. 4, 6024–6034, [arXiv:2303.13840 \[gr-qc\]](#).
- [60] S. Capozziello, G. Sarracino, and G. De Somma, “A Critical Discussion on the H_0 Tension,” *Universe* **10** (2024) no. 3, 140, [arXiv:2403.12796 \[gr-qc\]](#).
- [61] E. D. Valentino *et al.*, “The CosmoVerse White Paper: Addressing observational tensions in cosmology with systematics and fundamental physics,” [arXiv:2504.01669 \[astro-ph.CO\]](#).
- [62] C. Misner, K. Thorne, and J. Wheeler, *Gravitation*. No. pt. 3 in *Gravitation*. W. H. Freeman, 1973. <https://books.google.com.mt/books?id=w4Gigq3tYlkC>.
- [63] D. Foreman-Mackey *et al.*, “emcee: The mcmc hammer,” *Publications of the Astronomical Society of the Pacific* **125** (2013) no. 925, 306–312, [arXiv:1202.3665 \[astro-ph.CO\]](#).
- [64] R. Jimenez and A. Loeb, “Constraining cosmological parameters based on relative galaxy ages,” *The Astrophysical Journal* **573** (2002) no. 1, 37–42, [arXiv:astro-ph/0106145 \[astro-ph.CO\]](#).
- [65] Z. Cong *et al.*, “Four new observational $H(z)$ data from luminous red galaxies in the Sloan Digital Sky Survey data release seven,” *Research in Astronomy and Astrophysics* **14** (2014) no. 10, 1221, [arXiv:1207.4541 \[astro-ph.CO\]](#). <https://dx.doi.org/10.1088/1674-4527/14/10/002>.
- [66] R. Jimenez *et al.*, “Constraints on the Equation of State of Dark Energy and the Hubble Constant from Stellar Ages and the Cosmic Microwave Background,” *The Astrophysical Journal* **593** (2003) no. 2, 622–629, [arXiv:astro-ph/0302560 \[astro-ph.CO\]](#).
- [67] M. Moresco *et al.*, “A 6% measurement of the Hubble parameter at $z \sim 0.45$: direct evidence of the epoch of cosmic re-acceleration,” *Journal of Cosmology and Astroparticle Physics* **2016** (2016) no. 05, 014–014, [arXiv:1601.01701 \[astro-ph.CO\]](#).
- [68] J. Simon, L. Verde, and R. Jimenez, “Constraints on the redshift dependence of the dark energy potential,” *Physical Review D* **71** (2005) no. 12, , [arXiv:astro-ph/0412269 \[astro-ph.CO\]](#).
- [69] M. Moresco *et al.*, “Improved constraints on the expansion rate of the Universe up to $z \sim 1.1$ from the spectroscopic evolution of cosmic chronometers,” *Journal of Cosmology and Astroparticle Physics* **2012** (2012) no. 08, 006–006, [arXiv:1201.3609 \[astro-ph.CO\]](#).
- [70] D. Stern *et al.*, “Cosmic chronometers: constraining the equation of state of dark energy. I: $H(z)$ measurements,” *Journal of Cosmology and Astroparticle Physics* **2010** (2010) no. 02, 008–008, [arXiv:0907.3149 \[astro-ph.CO\]](#).
- [71] M. Moresco, “Raising the bar: new constraints on the Hubble parameter with cosmic chronometers at $z \sim 2$,” *Monthly Notices of the Royal Astronomical Society* **450** (2015) no. 1, 16–20, [arXiv:1503.01116 \[astro-ph.CO\]](#).
- [72] M. Moresco *et al.*, “Setting the stage for cosmic chronometers. ii. impact of stellar population synthesis models systematics and full covariance matrix,” *The Astrophysical Journal* **898** (2020) no. 1, 82, [arXiv:2003.07362 \[astro-ph.CO\]](#).
- [73] D. Brout *et al.*, “The Pantheon+ Analysis: SuperCal-fragilistic Cross Calibration, Retrained SALT2 Light-curve Model, and Calibration Systematic Uncertainty,” *The Astrophysical Journal* **938** (2022) no. 2, 111, [arXiv:2112.03864 \[astro-ph.CO\]](#).
- [74] D. Scolnic *et al.*, “The Pantheon+ Analysis: The Full Data Set and Light-curve Release,” *The Astrophysical Journal* **938** (2022) no. 2, 113, [arXiv:2112.03863 \[astro-ph.CO\]](#).
- [75] A. Conley *et al.*, “Supernova constraints and systematic uncertainties from the first three years of the supernova legacy survey,” *The Astrophysical Journal Supplement Series* **192** (2010) no. 1, 1, [arXiv:1104.1443 \[astro-ph.CO\]](#).
- [76] F. Beutler *et al.*, “The 6dF Galaxy Survey: baryon acoustic oscillations and the local Hubble constant: 6dFGS: BAOs and the local Hubble constant,” *Monthly Notices of the Royal Astronomical Society* **416** (2011) no. 4, 3017–3032, [arXiv:1106.3366 \[astro-ph.CO\]](#).
- [77] H. du Mas des Bourboux *et al.*, “Baryon acoustic oscillations from the complete SDSS-III Ly α -quasar cross-correlation function at $z = 2.4$,” *Astronomy & Astrophysics* **608** (2017) A130, [arXiv:1708.02225 \[astro-ph.CO\]](#).
- [78] A. J. Ross *et al.*, “The clustering of the SDSS DR7 main Galaxy sample I. A 4 per cent distance measure at $z=0.15$,” *Monthly Notices of the Royal Astronomical Society* **449** (2015) no. 1, 835–847, [arXiv:1409.3242 \[astro-ph.CO\]](#).
- [79] G.-B. Zhao *et al.*, “The clustering of the sdss-iv extended baryon oscillation spectroscopic survey dr14 quasar sample: a tomographic measurement of cosmic structure growth and expansion rate based on optimal redshift weights,” *Monthly Notices of the Royal Astronomical Society* **482** (2018) no. 3, 3497–3513, [arXiv:1801.03043 \[astro-ph.CO\]](#).

- [80] D. J. Fixsen, “The temperature of the cosmic microwave background,” *The Astrophysical Journal* **707** (2009) no. 2, 916–920, [arXiv:0911.1955 \[astro-ph.CO\]](#).
- [81] A. Lue, R. Scoccimarro, and G. D. Starkman, “Probing Newton’s constant on vast scales: Dvali-Gabadadze-Porrati gravity, cosmic acceleration, and large scale structure,” *Physical Review D* **69** (2004) no. 12, , [arXiv:astro-ph/0401515 \[astro-ph.CO\]](#).
- [82] E. V. Linder, “Cosmic growth history and expansion history,” *Physical Review D* **72** (2005) no. 4, , [arXiv:astro-ph/0507263 \[astro-ph.CO\]](#).
- [83] J.-P. Uzan, “The acceleration of the universe and the physics behind it,” *General Relativity and Gravitation* **39** (2007) no. 3, 307–342, [arXiv:astro-ph/0605313 \[astro-ph.CO\]](#).
- [84] R. Gannouji, B. Moraes, and D. Polarski, “The growth of matter perturbations in $f(R)$ models,” *Journal of Cosmology and Astroparticle Physics* **2009** (2009) no. 02, 034–034, [arXiv:0809.3374 \[astro-ph.CO\]](#).
- [85] S. Tsujikawa, K. Uddin, and R. Tavakol, “Density perturbations in $f(R)$ gravity theories in metric and Palatini formalisms,” *Physical Review D* **77** (2008) no. 4, , [arXiv:0712.0082 \[astro-ph.CO\]](#).
- [86] S. Basilakos, S. Nesseris, and L. Perivolaropoulos, “Observational constraints on viable $f(r)$ parametrizations with geometrical and dynamical probes,” *Physical Review D* **87** (2013) no. 12, , [arXiv:1302.6051 \[astro-ph.CO\]](#).
- [87] F. K. Anagnostopoulos, S. Basilakos, and E. N. Saridakis, “Bayesian analysis of $f(T)$ gravity using $f\sigma_8$ data,” *Physical Review D* **100** (2019) no. 8, , [arXiv:1907.07533 \[astro-ph.CO\]](#).
- [88] P. J. E. Peebles, *Principles of Physical Cosmology*, Princeton University Press, Princeton New Jersey. 1993.
- [89] J. Solà, A. Gómez-Valent, and J. de Cruz Pérez, “The H_0 tension in light of vacuum dynamics in the Universe,” *Phys. Lett. B* **774** (2017) 317–324, [arXiv:1705.06723 \[astro-ph.CO\]](#).
- [90] M. Gonzalez-Espinoza, G. Otalora, J. Saavedra, and N. Videla, “Growth of matter overdensities in non-minimal torsion-matter coupling theories,” *Eur. Phys. J. C* **78** (2018) no. 10, 799, [arXiv:1808.01941 \[gr-qc\]](#).
- [91] A. Gómez-Valent and J. Solà Peracaula, “Density perturbations for running vacuum: a successful approach to structure formation and to the σ_8 -tension,” *Mon. Not. Roy. Astron. Soc.* **478** (2018) no. 1, 126–145, [arXiv:1801.08501 \[astro-ph.CO\]](#).
- [92] A. De Felice and S. Tsujikawa, “ $f(R)$ theories,” *Living Rev. Rel.* **13** (2010) 3, [arXiv:1002.4928 \[gr-qc\]](#).
- [93] L. Kazantzidis and L. Perivolaropoulos, “Evolution of the $f\sigma_8$ tension with the Planck15/ Λ CDM determination and implications for modified gravity theories,” *Phys. Rev. D* **97** (2018) no. 10, 103503, [arXiv:1803.01337 \[astro-ph.CO\]](#).
- [94] Di Valentino, Eleonora and others, “Reducing the H_0 and σ_8 tensions with dark matter-neutrino interactions,” *Physical Review D* **97** (2018) no. 4, , [arXiv:1710.02559 \[astro-ph.CO\]](#).
- [95] V. Poulin, J. L. Bernal, E. D. Kovetz, and M. Kamionkowski, “Sigma-8 tension is a drag,” *Physical Review D* **107** (2023) no. 12, , [arXiv:2209.06217 \[astro-ph.CO\]](#).
- [96] S. Capozziello *et al.*, “Cosmographic bounds on the cosmological deceleration-acceleration transition redshift in $f(\mathcal{R})$ gravity,” *Phys. Rev. D* **90** (2014) 044016, [arXiv:1403.1421 \[gr-qc\]](#).
- [97] D. Camarena and V. Marra, “Local determination of the hubble constant and the deceleration parameter,” *Phys. Rev. Res.* **2** (2020) 013028, [arXiv:1906.11814 \[astro-ph.CO\]](#).
- [98] V. Sahni, A. Shafieloo, and A. A. Starobinsky, “Two new diagnostics of dark energy,” *Phys. Rev. D* **78** (2008) 103502, [arXiv:0807.3548 \[astro-ph.CO\]](#).
- [99] V. Sahni *et al.*, “Statefinder-a new geometrical diagnostic of dark energy,” *Journal of Experimental and Theoretical Physics Letters* **77** (2003) no. 5, 201–206, [arXiv:astro-ph/0201498 \[astro-ph.CO\]](#).